Journal of Alloys and Compounds 939 (2023) 168751

Contents lists available at ScienceDirect

Journal of Alloys and Compounds

journal homepage: www.elsevier.com/locate/jalcom

The influence of Sb doping on the local structure and disorder in thermoelectric ZnO:Sb thin films

Joana M. Ribeiro [a], Frederico J. Rodrigues [a], Filipe C. Correia [a], Inga Pudza [b], Alexei Kuzmin [b], Aleksandr Kalinko [c], Edmund Welter [c], Nuno P. Barradas [d,e], Eduardo Alves [d], Alec P. LaGrow [f], Oleksandr Bondarchuk [f], Alexander Welle [g], Ahmad Telfah [h], Carlos J. Tavares [*,a]

[a] Physics Centre of Minho and Porto Universities (CF-UM-PT), University of Minho, 4804-533 Guimarães, Portugal
[b] Institute of Solid State Physics, University of Latvia, LV-1063 Riga, Latvia
[c] Deutsches Elektronen-Synchrotron DESY – A Research Centre of the Helmholtz Association, Notkestraße 85, D-22607 Hamburg, Germany
[d] Institute of Plasma and Nuclear Fusion, Technical Superior Institute, University of Lisbon, 2695-066 Bobadela LRS, Portugal
[e] Centro de Ciências e Tecnologias Nucleares, Instituto Superior Técnico, Universidade de Lisboa, Estrada Nacional 10, 2695-066 Bobadela LRS, Portugal
[f] International Iberian Nanotechnology Laboratory, 4715-330 Braga, Portugal
[g] Institute of Functional Interfaces (IFG) and Karlsruhe Nano Micro Facility (KNMFi), Karlsruhe Institute of Technology (KIT), D-76344 Karlsruhe, Germany
[h] Leibniz Institut für Analytische Wissenschaften-ISAS-e.V., Bunsen-Kirchhoff-Straße 11, 44139 Dortmund, Germany

ARTICLE INFO

Article history:
Received 15 November 2022
Received in revised form 30 December 2022
Accepted 3 January 2023
Available online 7 January 2023

Keywords:
Antimony
Doped zinc oxide
Thin films
Sputtering
Thermoelectric
X-ray absorption

ABSTRACT

Thermoelectric transparent ZnO:Sb thin films were deposited by magnetron sputtering, with Sb content varying between 2 and 14 at%. As evidenced by X-ray diffraction analysis, the films crystallize in the ZnO wurtzite structure for lower levels of Sb-doping, developing a degree of amorphization for higher levels of Sb-doping. Temperature-dependent (10–300 K) X-ray absorption spectroscopy studies of the produced thin films were performed at the Zn and Sb K-edges to shed light on the influence of Sb doping on the local atomic structure and disorder in the ZnO:Sb thin films. The analysis of the Zn K-edge EXAFS spectra by the reverse Monte Carlo method allowed to extract detailed and accurate structural information in terms of the radial and bond angle distribution functions. The obtained results suggest that the introduction of antimony to the ZnO matrix promotes static disorder, which leads to partial amorphization with very small crystallites (~3 nm) for large (12–14 at%) Sb content. Rutherford backscattering spectrometry (RBS) experiments enabled the determination of the in-depth atomic composition profiles of the films. The film composition at the surfaces determined by X-ray photoelectron spectroscopy (XPS) matches that of the bulk determined by RBS, except for higher Sb-doping in ZnO films, where the concentration of oxygen determined by XPS is smaller near the surface, possibly due to the formation of oxygen vacancies that lead to an increase in electrical conductivity. Traces of Sb–Sb metal bonds were found by XPS for the sample with the highest level of Sb-doping. Time-of-flight secondary ion mass spectrometry obtained an Sb/Zn ratio that follows that of the film bulk determined by RBS, although Sb is not always homogeneous, with samples with smaller Sb content (2 and 4 at% of Sb) showing a larger Sb content closer to the film/substrate interface. From the optical transmittance and reflectance curves, it was determined that the films with the lower amount of Sb doping have larger optical band-gaps, in the range of 2.9–3.2 eV, while the partially amorphous films with higher Sb content have smaller band-gaps in the range of 1.6–2.1 eV. Albeit the short-range crystalline order (~3 nm), the film with 12 at% of Sb has the highest absolute Seebeck coefficient (~56 μV/K) and a corresponding thermoelectric power factor of ~0.2 $\mu W \cdot K^{-2} \cdot m^{-1}$.

© 2023 The Author(s). Published by Elsevier B.V. This is an open access article under the CC BY-NC-ND license (http://creativecommons.org/licenses/by-nc-nd/4.0/).

1. Introduction

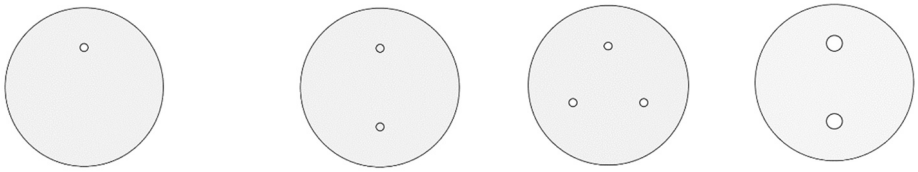
ZnO-based thin films have found in the last years a surge in applications as transparent conductive oxide electrodes [1,2], thermoelectric films [3–6], and gas sensors [7,8], amongst other applications, due to the inherent semiconductor, electric, optical and thermal properties of these materials. In order to have enhanced

* Corresponding author.
E-mail address: ctavares@fisica.uminho.pt (C.J. Tavares).

https://doi.org/10.1016/j.jallcom.2023.168751
0925-8388/© 2023 The Author(s). Published by Elsevier B.V. This is an open access article under the CC BY-NC-ND license (http://creativecommons.org/licenses/by-nc-nd/4.0/).

Table 1
Produced ZnO:Sb thin films with respective compositions (determined from RBS experiments) and thickness.

Specification		Sample Denomination				
		UE	**UT**	**UF**	**UC**	**UD**
		ZnO:Sb	ZnO:Sb:N	ZnO:Sb	ZnO:Sb	ZnO:Sb
Composition [RBS]	**Sb (at%)**	2	2	4	12	14
	N (at%)	–	< 2	–	–	–
Thickness (nm)		490	560	230	780	620
Sb pellets position in ZnO target		Ø5 mm pellets x 1		Ø5 mm pellets x 2	Ø5 mm pellets x 3	Ø10 mm pellets x 2



thermoelectric efficiency, these materials need to have a low thermal conductivity, high electric conductivity, and a high Seebeck coefficient, and preferably produced at a lower dimension [9–11]. An enhancement of the electric [2,12,13] and thermoelectric [14,15] properties is attained by suitably doping ZnO with anions or cations that are soluble in the wurtzite structure. Further improvement in the thermoelectric properties can be achieved by doping ZnO with cations with larger ionic radii that act as phonon dispersion centres thus facilitating the reduction of thermal conductivity [16–18], such as antimony or bismuth with ionic radii of 0.80 Å and 1.03 Å respectively, much greater than that of zinc (0.60 Å). This thermoelectric effect is much larger for doped-ZnO bulk or nanocomposites materials. For example, regarding ZnO-based nanostructured ceramic pellets at 300 K, there are reports of absolute Seebeck coefficients of ~500 μV/K for ZnO:Bi and ZnO:Al, ~300 μV/K ZnO:In, and ~200 μV/K for ZnO:Ga [14,16,19,20]. As a comparison, much smaller absolute Seebeck coefficients have been obtained at 300 K for doped-ZnO transparent thin films deposited at low temperature (< 473 K): ZnO:Al (~35 μV/K), ZnO:Ga (~30 μV/K), ZnO:Sb (~25 μV/K), ZnO:Al,Bi (~50 μV/K), ZnO:Ga,Bi (~40 μV/K), ZnO:Sb (40–60 μV/K) [17,18,21,22].

The motivation of this work is to produce thermoelectric transparent ZnO:Sb thin films envisaging low-temperature thermal energy harvesting applications, such as tactile displays, solar cells, and window panes, amongst other structures and devices, where the thermal gradient is generally below 10 K. For this, ZnO:Sb films were deposited by magnetron sputtering, with Sb content varying in the range of 2–14 at%. Rutherford backscattering spectrometry (RBS) and X-ray photoelectron spectroscopy (XPS) were used to assess the bulk and surface composition of the grown films, respectively. Time-of-Flight Secondary Ion Mass Spectrometry (ToF-SIMS) was used to analyse the bulk homogeneity of the films. X-ray diffraction (XRD) was used to study the developed crystallographic phases, while scanning electron microscopy (SEM) was adopted to observe the film surface and cross-section microstructure. High-resolution electron microscopy (HRTEM) combined with energy-dispersive X-ray spectroscopy (EDX) enabled the observation of the crystalline grains and identify their composition and lattice parameters. Temperature-dependent (10–300 K) X-ray absorption spectroscopy study of the produced ZnO:Sb thin films was performed to determine the coordination environment of Sb dopant atoms and their influence on the local atomic structure and lattice dynamics of the ZnO matrix. These experiments were correlated with the electric and optical characterization.

2. Materials and methods

Antimony-doped zinc oxide (ZnO:Sb) thin films were prepared by magnetron sputtering, using a home-made system (Fig. A1, Appendix). A 99.95% purity ZnO target was used (FHR Anlagenbau GmbH, Germany), loaded with 99.95% purity Sb pellets with 10 mm diameter and 2 mm thickness (Goodfellow, UK). In order to control the Sb content, the position of the Sb pellets in the ZnO target was adjusted (see Table 1). Smaller 5 mm diameter pellets refer to pellets re-used after a few depositions, as they decreased in size due to deposition erosion, which allowed for finer control of Sb-doping. These films were deposited on 25 mm × 75 mm glass slides (Normax, Portugal), 10 mm × 10 mm Si substrates with < 100 > orientation (SIEGERT WAFER GmbH, Part-No: L14016) and 10 mm × 10 mm Kapton® film. All substrates were previously cleaned with isopropanol in an ultrasound bath for 15 min. Prior to deposition, the substrates were etched in an Ar^+ plasma at 2 Pa to further clean the exposed surfaces. The substrates were fixed with Kapton tape to a sample holder, radially symmetrical to the centre of the target, with a 90 mm target-to-substrate distance. The films were deposited with a target current density of 5.0 mA·cm^{-2}, a deposition temperature of 473 K, an argon (working gas) flow of 40 sccm, which corresponds to a working pressure of 0.37 Pa, and an isolated substrate bias of −60 V. The vacuum deposition chamber was baked with external sleeves for an hour before the deposition, in order to reduce the base pressure for each deposition (~10^{-4} Pa). For one particular sample, UT (see Table 1) a small amount of nitrogen was introduced during deposition, with a partial pressure of 0.02 Pa. After deposition, in order to enhance the microstructure of the ZnO:Sb films, the films were annealed in a vacuum furnace at 10^{-3} Pa and 573 K for 1 h and then cooled to room temperature.

High-resolution transmission electron microscopy, high-angle annular dark-field scanning transmission electron microscopy (HAADF-STEM), bright field scanning transmission electron microscopy (BF-STEM), and EDX analyses were carried out for ZnO:Sb thin films deposited on Si substrates at the International Iberian Nanotechnology Laboratory (INL), Braga, Portugal. For this, a FEI Model Titan Themis 60–300 electron microscope was used equipped with a field emission gun (X-FEG), Cs image and probe corrector, and super X EDX detectors, operating at 200 kV. Lamellae preparation was performed with a FEI Helios NanoLab 450 S Focus Ion Beam equipment, operating with a Ga gun. Due to this type of gun, Ga could not be atomically quantified in the analysed films. SEM analyses were performed on a FEI Nova 200 FEG-SEM at SEMAT/UM, University of Minho.

A Bruker AXS D8 Discover system (SEMAT/UM, University of Minho) equipped with a copper anode X-ray tube (CuK_α radiation) was used for XRD in the grazing incidence geometry (incident at $\theta = 1.000^\circ$) to probe the crystallinity, texture, and phase composition of the films grown on Si substrates.

The surface chemistry of the produced ZnO:Sb films was studied with an XPS spectrometer (Kratos Axis-Supra instrument, at 3Bs Group, University of Minho) equipped with a monochromatic Al-Kα X-ray radiation source (1486.6 eV) operated at an X-ray power of 225 W. The photoelectron spectra were collected at the take-off angle of 90º with the sample surface by means of a hemispherical electron energy analyser operated in the constant analyser energy lens mode (CAE). The pass energy of 160 eV and 40 eV was used for the survey and high-resolution spectra, respectively. The binding energy was referenced by setting the binding energy of the C1s hydrocarbon peak (the most intensive component of the C1s spectrum) at 284.8 eV. An electron flood gun was used to compensate for surface charging effects.

RBS experiments were carried out at Centro de Ciências e Tecnologias Nucleares, Instituto Superior Técnico in Lisbon, Portugal. The RBS data were analysed with the IBA DataFurnace NDF v10.0a [23]. Double scattering was calculated with the algorithms given in [24]. Pileup was calculated with the algorithms given in [25]. For each sample, a layered profile was determined through automatic fits to the spectra. Point-by-point profiles, where from each data point a concentration value is calculated, were also derived. The layered profiles show the layers without roughness. However, to fit the present experimental data, a roughness profile was added to take into account interdiffusion phenomena. Point-by-point profiles are complex because they are calculated directly from the counts of each element in each channel. For example, on the surface of the film, the Sb signal is clear and the calculation is direct and correct. However, across the film, further from the surface, the Sb signal overlaps the Zn signal. The NDF software subtracts the calculated partial spectra of the other elements from the experimental data, leaving what corresponds to the X element. In most samples, the fit is improved when a thin layer without Sb is present near the interface with the Si substrate. This may indicate the formation of an oxide interlayer during the first moments of deposition.

TOF-SIMS was performed on a TOF.SIMS5 spectrometer (ION-TOF GmbH, Münster, Germany) equipped with a Bi cluster primary ion source and a non-linear time-of-flight analyser, at the Institute of Functional Interfaces (IFG), Karlsruhe Institute of Technology (KIT), Germany. Ultra-high vacuum base pressure was $< 2 \times 10^{-8}$ mbar. The primary ion source was operated in "high current bunched" mode providing short Bi^+ primary ion pulses 0.8 ns / 25 keV energy, a lateral resolution of approximately 4 µm, and a target current of 1.4 pA. For depth profiling a dual beam analysis was performed in interlaced mode: the primary ion source was scanned over an area of $300 \times 300\ \mu m^2$ (128 × 128 data points), and a sputter gun was scanned over a concentric field of view. For positive polarity profiles, a O_2^+ beam was applied to erode the sample, with 2 keV sputter energy, at 45° incident angle, a scan range of $600 \times 600\ \mu m^2$ and a target current of approximately 500 nA. For negative polarity profiles, a Cs^+ beam eroded the sample, with 2 keV sputter energy, a scan range of $500 \times 500\ \mu m^2$, and target current of approximately 100 nA. Since the data acquisition is fast in respect of the observed erosion speeds, 25 data points were binned for plotting. Secondary ion intensities are plotted over depth, using thickness obtained through cross-section Scanning Electron Microscopy images. Note however that this scale is not linear if different materials with different erosion rates/sputter yields are analysed.

For the study of the optical properties, the analysis of reflectance and transmittance of the films was performed on a Shimadzu Absorption Spectrophotometer, Model UV-2501 PC. The Seebeck Coefficient was evaluated in custom-made equipment operated in a vacuum (1 Pa) in the temperature range of 293–343 K. The system is based on the Seebeck effect, using a direct conversion of a temperature gradient into electrical voltage to measure the Seebeck coefficient. Two Peltier cells are used at each edge of the sample (75 mm × 25 mm), for cooling and heating opposite edges and hence perform a thermal gradient across the film surface. The generated voltage is proportional to the temperature difference between the hot and cold ends of the sample. For the study of the electrical properties of the produced samples, an Ecopia HMS-5000 Hall Effect Measurement System with automated magnet movement and variable temperature capability was used. The operation of this equipment is based on the four-point method proposed by Van der Pauw in 1958 [26], which allows for estimating the electrical conductivity of a film through the ratio between the film thickness and the sheet resistance.

Temperature-dependent X-ray absorption spectra were measured at the P65 Applied XAFS beamline [27] of the HASYLAB/DESY PETRA III storage ring, operated at energy $E = 6.08$ GeV and current $I = 100$ mA in top-up 40 bunch mode. The harmonic reduction was achieved by uncoated and Pt-coated silicon plane mirrors. Fixed exit double-crystal monochromators Si(111) and Si(311) were used for the Zn (9659 eV) and Sb (30,491 eV) K-edges, respectively. X-ray absorption spectra were collected in transmission mode using two ionization chambers. The Oxford Instruments liquid helium flow cryostat was used to maintain the required sample temperature in the range of 10–300 K. Thin film ZnO:*x*Sb samples deposited on Kapton were packed in stacks. Four reference samples (ZnO and Sb_2O_5 powders, Zn and Sb foils) were used for energy scale calibration and comparison.

Experimental X-ray absorption spectra were treated using the XAESA code [28] following a conventional procedure [29]. Both X-ray absorption near edge structure (XANES) and extended X-ray absorption fine structure (EXAFS) parts were extracted. A qualitative analysis of the XANES spectra at the K-edges of Zn and Sb was carried out by comparing the spectra of thin films with the XANES spectra calculated for various cluster sizes for ZnO in [30] and measured for reference compounds (Sb foil and Sb_2O_5). EXAFS spectra at both edges were analysed using two theoretical approaches. The contributions from the first and second coordination shells of Zn, composed of oxygen and zinc atoms, respectively, and the first coordination shell of Sb, composed of oxygen atoms, were analysed using the conventional EXAFS equation within the single-scattering approximation [29,31]. The required backscattering amplitude and phase shift functions for Zn–O, Zn–Zn, and Sb–O atom pairs were calculated using ab initio self-consistent real-space multiple-scattering (MS) FEFF 8.50 L code [32,33]. The scattering potential and partial phase shifts were calculated within the muffin-tin (MT) approximation [32,33] for the clusters constructed based on the crystallographic structures of reference compounds with a radius of 8 Å, centred at the absorbing (Zn or Sb) atom. The inelastic losses of a photoelectron were accounted for using the complex exchange-correlation Hedin-Lundqvist potential [34]. The amplitude reduction factor S_0^2 was included in the scattering amplitude [32,33], and no additional EXAFS amplitude correction was performed.

The reverse Monte Carlo (RMC) method with the evolutionary algorithm (EA) approach implemented in the EvAX code [35] was employed to extend the EXAFS analysis at the Zn K-edge up to the distant coordination shells (up to 5.6 Å). This method was successfully used in the past to determine the local atomic structure and its temperature dependence in zinc oxides [35,36] and Nb-doped titanium dioxide [37]. In the RMC/EA method, a large simulation box filled with atoms (supercell) is first built based on the crystallographic structure of the material. Next, at each RMC iteration, a new configuration of atoms is generated by randomly displacing all the atoms in the simulation box. The maximum allowable

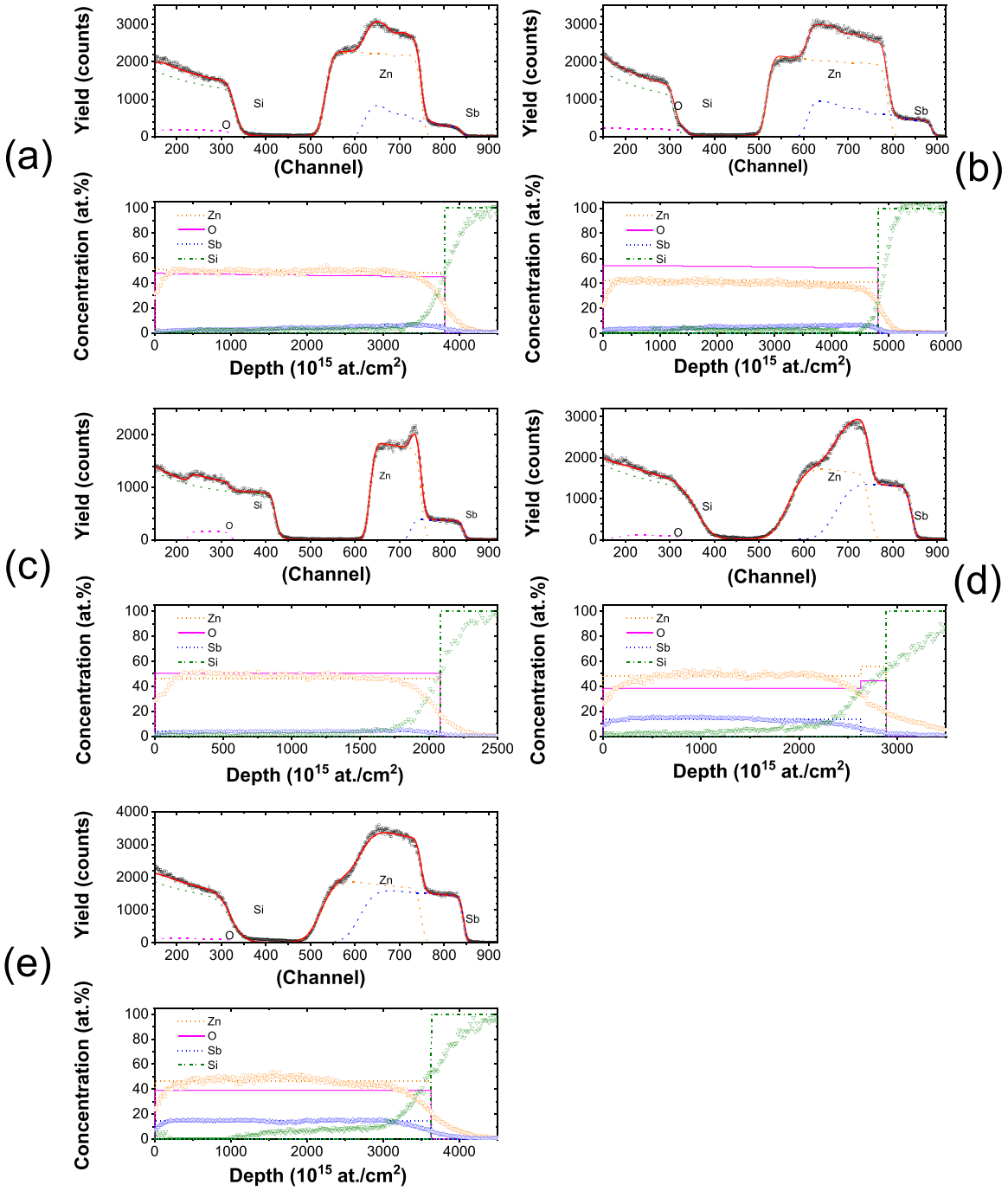


Fig. 1. RBS experimental data and respective fits and in-depth composition profiles for ZnO:Sb thin films with varying Sb content: a) 2 at%, b) 2 at% and N < 2 at%, c) 4 at%, d) 12 at % and e) 14 at%.

displacement of atoms was limited to 0.4 Å to avoid too large instant structural changes. The agreement between the Morlet wavelet transforms (WTs) of the experimental and calculated configuration-averaged EXAFS spectra was used as a criterion for accepting the new atomic configuration. The use of the wavelet transform ensures a good agreement between experiment and theory in both *k*- and *R*-spaces simultaneously. The coordinates of atoms in the final configuration were used to calculate a set of radial distribution functions (RDFs) for the required atom pairs, which were further used to obtain structural parameters such as coordination numbers (*N*), interatomic distances (*R*), and mean-square relative displacements (MSRDs) (σ^2), also known as the Debye-Waller factors. Since RMC simulations are performed up to distant shells, the multiple-scattering (MS) contributions to the configuration-averaged EXAFS spectra must be taken into account by using the FEFF 8.50 L code [32,33].

3. Results and discussion

3.1. Composition profiles

Table 1 summarizes the produced ZnO:Sb thin films taking into account the varying Sb doping content in ZnO, and respective film thickness. The registered compositions were derived from the fits to

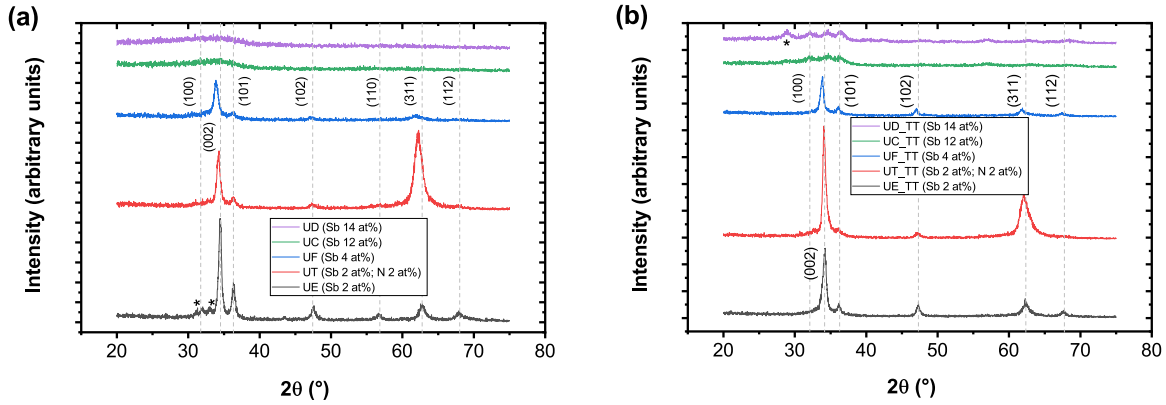


Fig. 2. Grazing incidence XRD patterns for the a) as-deposited and b) post-deposition thermal treated in vacuum ZnO thin films with varying Sb content; * denotes a $Zn_7Sb_2O_{12}$ orthorhombic phase.

the RBS data, while the thickness was assessed from the observation of the cross-section in SEM micrographs, as seen in Section 3.3. Throughout the manuscript, the samples are presented and labelled according to their composition measured by RBS.

Fig. 1 presents the RBS experimental spectra and respective fits along with the in-depth atomic composition profiles for all ZnO:Sb films, with varying Sb content. For all samples, Zn is slightly depleted in the topmost atomic layers. In the case of 2 at% of Sb doping (UE. Fig. 1a), Zn varies in-depth in the range of 48–51 at%, while O is slightly deficient, varying between 45 and 48 at%. With an increment to 4 at% of Sb doping in ZnO (UF, Fig. 1c), O is practically constant at 50 at% and Zn is slightly depleted in-depth, varying from 46 to 47 at %. For the largest levels of Sb doping, 12 and 14 at% (UC and UD, Fig. 1d-e), a large contribution from this element arises in the RBS experimental spectra and O decreases sharply to the range of 38–39 at%, while Zn varies between 47 and 48 at%. In general, the Sb content is approximately constant in-depth in all films, but an increase at the film/substrate interface is apparent due to diffusion. This diffusion is most noticeable for the sample with 2 at% of doping (Fig. 1a), where Sb is stable at that composition in the bulk but increases up to ~6 at% towards the film–silicon substrate interface. Also in Fig. 1b) is a plot for the ZnO:Sb (2 at%) film with N doping (< 2 at%). Besides the O signal overlapping that of N, the spectra and in-depth composition are very similar to that of ZnO:Sb (2 at%) film without N doping.

3.2. Crystallinity

Fig. 2a) presents grazing incidence X-ray diffraction patterns for the as-deposited ZnO:Sb thin films. All diffraction peaks are assigned to a ZnO phase with hexagonal wurtzite crystal structure, $P6_3mc$ (186) space group, ICDD crystallographic card 01–070–8070. The films with a larger concentration of Sb (UC with 12 at%, and UD with 14 at%) do not evidence a relevant crystallinity. Conversely, the films with lower Sb amount are crystalline, with a preferred orientation along [001] for UE (Sb 2 at%) and UF (Sb 4 at%). For the latter films, the most intense diffraction comes from the (002), (101), and (112) atomic planes. The diffraction peak positions for sample UE (Sb 2 at %) match those of the aforementioned crystallographic card, with lattice parameters a= 3.245 Å and c= 5.205 Å, while for UF (Sb 4 at%) and UT (Sb 2 at%; N 2 at%) the diffraction peaks are slightly shifted towards smaller Bragg angles, indicating an out-of-plane lattice expansion. With nitrogen doping, in UT, a more pronounced texture along [103] is discerned. These as-deposited films were subjected to thermal annealing in a vacuum, and the resultant XRD patterns are displayed in Fig. 2b). The resulting treatment at 473 K developed a higher crystallinity in all films. The as-deposited films with a higher Sb content, show minor traces of the development of a polycrystalline structure, albeit with much smaller intensity than the films with less Sb doping. Noteworthy to mention is the appearance of very low-intensity diffraction peaks at 2θ = 31.2º and 33.0º for the as-deposited film with the lowest content of Sb (UE), assigned to the orthorhombic space group Cmme (67) β-$Zn_7Sb_2O_{12}$ phase [38] (marked with an asterisk). The latter peaks are absent for the heat-treated sample, as well on sample UT with similar Sb-doping but with N-doping. For the thermal-treated sample with the highest Sb doping (UD_TT), an additional low-intensity diffraction peak is present at 28.9º, assigned to the aforementioned β-$Zn_7Sb_2O_{12}$ phase (marked with an asterisk).

3.3. Electron microscopy analysis

The surface and cross-sectional morphology of the as-deposited ZnO:Sb thin films was studied (Fig. A2). The samples with the highest concentration of antimony (UC and UD) grow without a structural order, developing large 3D dome-shaped grains, with relatively large pores between them. On the other hand, the samples with lower Sb content (UE, UF, and UT) develop a distinct columnar morphology comprising polycrystalline grains that broaden in the direction of the film growth.

STEM/HAADF cross-sectional micrographs with chemical element maps were obtained for ZnO:Sb films with Sb 2 at% (UE, Fig. A3a), 4 at% (UF, Fig. A3b), and Sb 14 at% (UD, Fig. A3c). The platinum signal comes from the FIB sample preparation process. From these micrographs it is apparent that the microstructure of the film with smaller Sb content (2 at%) has large V-shaped 3D grains, that enlarge from the substrate to the surface of the film, with a homogenous composition (Fig. A3 a). The aforementioned morphology of the V-shaped grains become less evident with further doping (4 at%) of Sb in ZnO (Fig. A3 b). Conversely, for the highest level of Sb doping (14 at%) (Fig. A3 c), segregation of Zn- and Sb- rich zones are discerned. This analysis corroborates with the XRD discussion inherent to Fig. 2. For the latter sample (UD, Sb 14 at%), the microstructure present in Fig. 3 reveals Sb-poor and -rich regions that result from the high doping in Sb, where phase segregation is evidenced, with distinct diffraction patterns. The Sb-poor region is more crystalline with domains of 1–3 nm attributed to the ZnO wurtzite crystal phase, as seen in the inset FFT outlined in red, where all spacings are ascribed to this structure. The atomic spacings from the Sb-rich side (outlined in blue) are less clear, and do not match the wurtzite structure, being most likely from underdeveloped $Zn_xSb_yO_z$ crystals in a surrounding amorphous matrix, as seen in the XRD patterns in Fig. 2. The phase segregation to the ZnO-rich side is typically closer to the Si substrate.

Additionally, the cross-sectional microstructure with the higher resolution was studied for the ZnO films with Sb 2 at% (UE, Fig. A4 a-

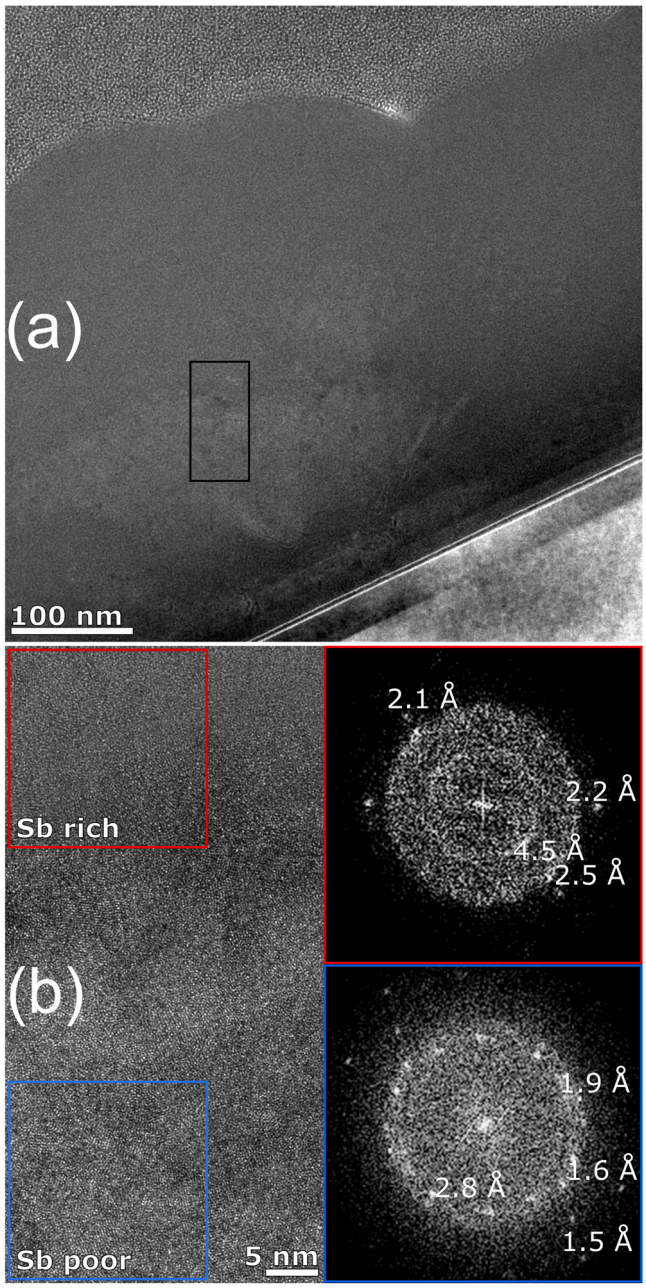


Fig. 3. STEM cross-sectional micrograph with inset FFTs of two selected zones for sample ZnO: Sb 14 at% (UD). (b) is a magnification of the region from (a) outlined by a black rectangle. In (b), the red and blue squares are representative of Sb-rich and Sb-poor regions, respectively.

b), Sb 4 at% (UF, Fig. A4 c-d) and Sb 14 at% (UD, Fig. 3). For each of these experiments, Fast Fourier Transform (FFT) images were registered reflecting the electron diffraction patterns of selected regions of interest delimited by squares in the micrographs. The aforementioned V-shaped 3D grains characteristic of sample ZnO:Sb 2 at% (UE) have an average size of ~200 nm (Fig. A4 a,b). The blue square in Fig. A4 b) is a magnification of the zone indicated by the black square in Fig. A4 a), being the FFT pattern indexed to the [111] zone axis of the ZnO wurtzite structure, since the lattice spacings of ~2.5 Å and 2.8 Å correspond to (101) and (100) atomic planes, respectively. Similarly, the blue square in Fig. A4 d) is a magnification of the zone indicated by the black square in Fig. A4 c), since the FFT pattern is indexed now to the [100] zone axis of the same structure.

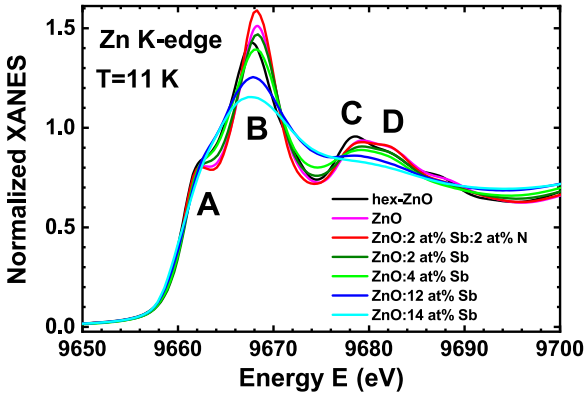


Fig. 4. Zn K-edges XANES spectra for hex-ZnO powder, undoped (ZnO), and Sb-doped ZnO thin films at 11 K.

3.4. X-ray absorption experiments

3.4.1. Zn K-edge

The experimental Zn K-edge XANES spectra measured at 11 K are compared in Fig. 4. Four main peaks (A-D) are resolved and vary strongly with the Sb content. Their origin is due to the photoelectron scattering by groups of atoms located at different distances around the absorbing zinc atom. Based on the ab initio full-multiple-scattering calculations, it was shown in [30] that the main peak B and the broad oscillation under the peaks C and D arise due to scattering by four oxygen atoms of the first coordination shell of zinc. The shoulder A and two peaks C and D appear when oxygen and zinc atoms located up to at least 4 Å around the absorber are considered [30]. This means that only short-range order is expected to exist in the ZnO:*x*Sb films with $x = 14$ at%, but the structure of the films is more ordered for small (0–4 at%) Sb content.

Experimental Zn K-edge EXAFS $\chi(k)k^2$ spectra and their Fourier transforms (FTs) at 11 K are compared for all samples in Fig. 5. Note that the peaks in all FTs reported here are located at distances that are slightly shorter than their crystallographic values because the FTs were not corrected for the phase shift present in the EXAFS equation. The analysis of the first two peaks in FTs was performed in detail. They correspond to the first coordination shell of zinc composed of oxygen atoms (the peak at about 1.5 Å) and to the second coordination shell of zinc composed of zinc atoms (the peak at about 3 Å) [31].

A strong decrease of all peak amplitude is well visible upon increasing Sb content due to a decrease in the film crystallinity. This result correlates well with our conclusion from XANES behaviour. Indeed, the peak ascribed to the second coordination shell (Zn–Zn) at 3 Å decreases significantly upon Sb doping and nearly disappears for $x = 14$ at%. When comparing samples UE and UT, with similar Sb-doping, the additional N-doping in UT promotes a higher amplitude of the oscillations due to reduced disorder in comparison with UE (without N-doping). The latter observation is interesting in indicating that a small quantity of N in the wurtzite lattice reduces structural disorder for the same level of Sb-doping.

The contributions from the first two coordination shells around Zn atoms were isolated by the Fourier filtering procedure in the *R*-range of 0.6–3.5 Å and fitted using the two-component model within the single-scattering harmonic approximation in the k-range of 2.5–14 $Å^{-1}$ [29]. During the fit, the values of the coordination numbers, the interatomic distances, and the MSRDs were allowed to vary. The interatomic distances in all samples turned out to be close and have the average values of R(Zn–O) = 1.97 ± 0.02 Å and R(Zn–Zn) = 3.25 ± 0.02 Å. From this, it was possible to extract values of MSRDs for Zn–O and Zn–Zn atom pairs in the first and second coordination

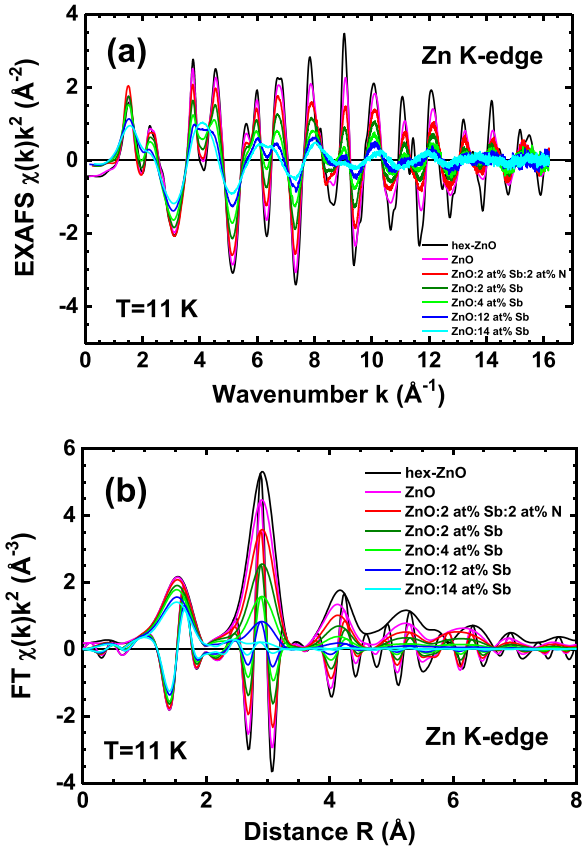


Fig. 5. (a) Experimental Zn K-edges EXAFS $\chi(k)k^2$ spectra and (b) their Fourier transforms (FTs) for hex-ZnO powder, undoped (ZnO), and Sb-doped ZnO thin films at 11 K.

shells of zinc, respectively (Fig. A5 a,b). The temperature dependencies of MSRDs for all samples are quite close, but the presence of static disorder in the thin film samples leads to an increase in the MSRD values upon increasing Sb content. Nevertheless, at high Sb content (x = 12 and 14 at%), the MSRD values for Zn–Zn atom pairs decrease unphysically due to a weak experimental signal and a correlation between MSRD and coordination number parameters. The composition dependence of the coordination numbers (N) of zinc in the first and second shells at 11 K was also determined (Fig. A5 c). For small Sb content, their values are close to that in crystalline ZnO. However, the strong disorder present in the samples for large Sb content results in an unphysical value (close to zero) of the coordination number in the second shell.

More detailed and accurate information on the local structure around zinc was obtained from the RMC/EA simulations based on the wurtzite-type ZnO structural model for two selected examples for ZnO:xSb (x = 2 and 14 at%) thin films at 11 and 293 K (Fig. A6). Good agreements between the experimental and calculated by RMC EXAFS spectra and their FTs were also achieved for the other temperatures and samples (not shown). The radial distribution functions (RDFs) for Zn–O and Zn–Zn atom pairs calculated from the coordinates of atoms located in the simulation RMC box are shown in Fig. 6. It is well visible that the static disorder induced by the presence of Sb dopant ions in the films dominates the thermal disorder effect. The first coordination shell of zinc composed of 4 oxygen atoms is well separated, while the peaks due to outer shells broaden and overlap at large Sb content.

The second moments of the RDFs or MSRDs were numerically calculated for the first two peaks, and their temperature dependencies were plotted (Fig. A7). The behaviour of the MSRDs obtained by the RMC method for the samples with low-Sb content is close to that in Fig. A5, which was calculated within the Gaussian model. However, there is a significant difference for the samples with high-Sb content: the RMC simulations predict more than 10 times larger values of MSRDs for the Zn–Zn distribution. To understand the origin of this effect, the bond angle distribution functions (BADFs) were calculated for the Zn–O–Zn angle in ZnO:xSb (x = 2 and 14 at%) thin films at 11 K, and the average values of the angles were obtained (Fig. A8): they are equal to 107 ± 4° for x = 2 and 111 ± 10° for x = 14. For comparison in wurtzite-type ZnO, the Zn–O–Zn angle is 108° for two Zn atoms in different hexagonal planes and 111° for two Zn atoms in the same hexagonal sheet [39]. Therefore, the average values of Zn–O–Zn angles in the films are close to that in the wurtzite phase, but their distributions increase.

To conclude, an increase in the variation of the bonding angle from 4° to 10° between adjacent [ZnO_4] tetrahedra connected by corners and the large values of the Zn–O MSRD (Fig. A7(a)), indicating distortions of [ZnO_4] tetrahedra, are responsible for the static disorder in ZnO films with a high content of antimony.

3.4.2. Sb K-edge

The experimental Sb K-edge XANES spectra measured at 293 K are compared in Fig. 7(a). The spectra for Sb foil and Sb_2O_5 powder give information on the absorption edge shift when the Sb oxidation state changes from 0 to 5 + . The shape of the XANES spectra of Sb-doped ZnO thin films is close to that of the oxide. However, the position of the absorption edge is located between those of the Sb foil and Sb_2O_5 suggesting an intermediate oxidation state for Sb ions. The XANES spectra of the films can be tentatively divided into two groups. In the first group, including the films with 12 at% and 14 at% of Sb, the oxidation state of antimony ions is slightly smaller than in the films of the second group, with a small amount (2 – 4 at%) of antimony.

A more accurate estimate of the Sb oxidation state in the films can be done by comparing the shift of the absorption edge relative to that of the Sb foil, estimated from the maximum of the first derivative of the X-ray absorption coefficient. In Fig. 7(b), we compare our data with those taken from [40] for a set of reference antimony oxides (Sb_2O_3, Sb_2O_4, and $FeSbO_4$). The intersection of horizontal lines with the dependence of the edge shift on the oxidation state of Sb provided us with the required information. As a result, the oxidation state of Sb in ZnO:14 at% Sb is about 3 + , it increases to about 4 + in ZnO:12 at% Sb, and finally becomes close to about 5 + in the other three samples with low Sb content.

Experimental Sb K-edge EXAFS $\chi(k)k^2$ spectra and their FTs for Sb-doped ZnO thin films were obtained at 11 K (Fig. 8). Two groups of spectra can be recognized: at low-Sb content (2 and 4 at%), the amplitude of the first peak in FT at 1.5 Å is larger than for high-Sb content (12 and 14 at%), while the amplitude of the second group of peaks at 2–3.5 Å is smaller. This fact suggests that Sb ions are located in a different local environment, which depends on the composition. Note that the Sb K-edges EXAFS spectra measured at higher temperatures are almost the same within the experimental noise as at 11 K suggesting strong dominance of the static disorder over the thermal one. As observed for the Zn-K edge, for the lower Sb-doped samples (UE and UT, 2 at%), N-doping in UT actually relaxes some of the disorder.

Since it is not known how Sb ions enter the ZnO matrix, the analysis of EXAFS spectra was performed based on the one-component model within the single-scattering approximation [29]. Examples of the best fits for two samples with low (2 at%) and high (14 at%) Sb content are shown in Fig. 9. The first peak in FTs was isolated using the inverse FT and best fitted considering one group of oxygen atoms. As a result of the best fits, it was found that Sb atoms are surrounded by 5–6 oxygen atoms at 1.95 ± 0.02 Å with the MSRD σ^2 = 0.004 ± 0.002 Å^2 in the ZnO:2–4 at% Sb thin films. Such an

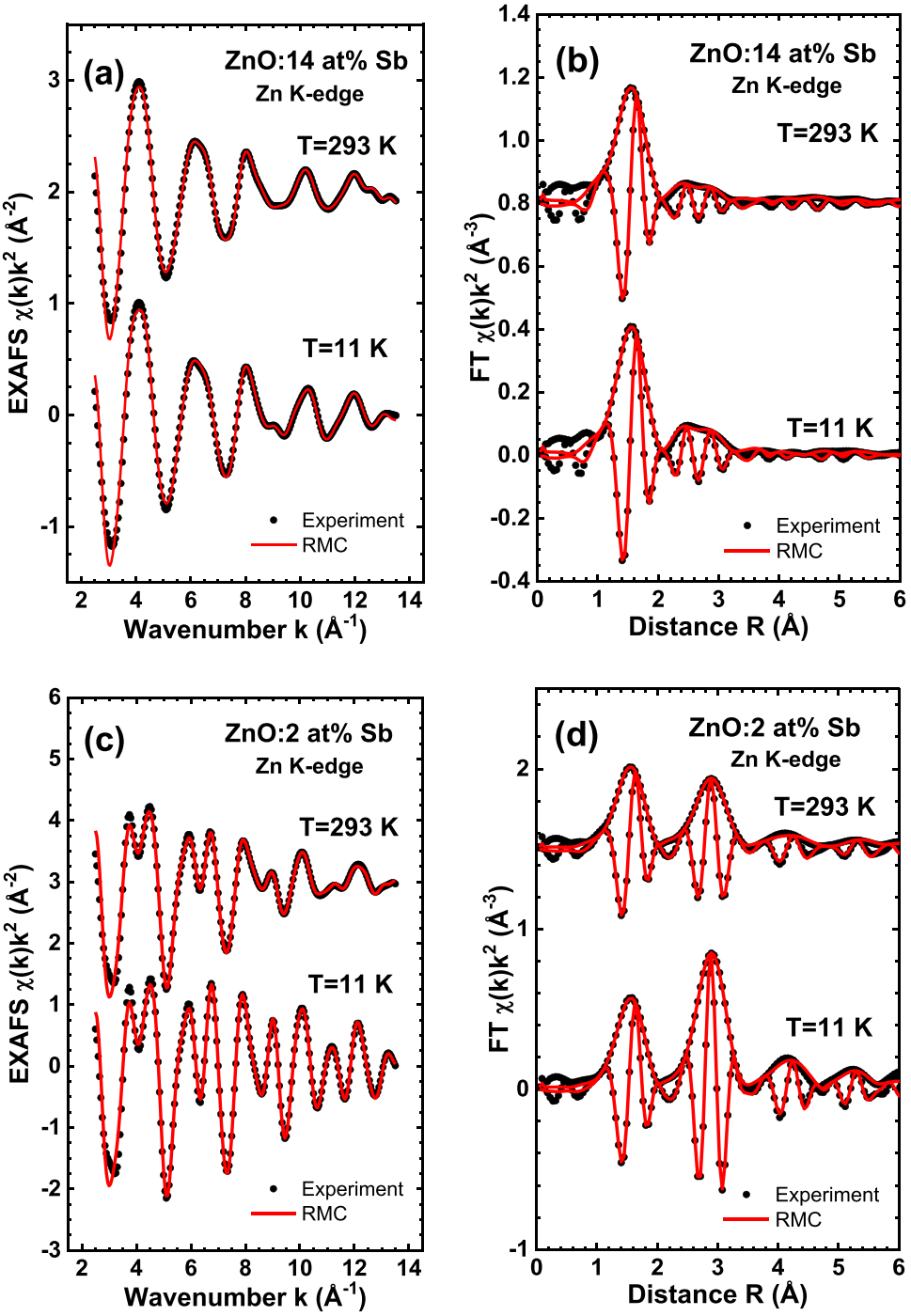


Fig. 6. Experimental and calculated by RMC Zn K-edges (a,c) EXAFS $\chi(k)k^2$ spectra and (b,d) their Fourier transforms (FTs) for ZnO:*x*Sb (*x* = 2 and 14 at%) thin films at 11 and 293 K.

environment is close to that in Sb_2O_5, where Sb ions are octahedrally coordinated with two groups of three oxygen atoms each located at 1.89–1.91 Å and 2.04–2.10 Å [41]. In disordered ZnO films with high (12 and 14 at%) Sb content, the local surrounding of Sb becomes different: there are only three oxygen atoms in the first shell located at about 1.95–1.96 Å with the MSRD $\sigma^2 = 0.005 \pm 0.002$ Å^2. Such coordination of antimony can be found in $ZnSb_2O_4$ [42], where it has an oxidation state 3 + . The Sb^{3+} ions with low coordination play the role of the network modifier and at sufficiently large concentrations promote amorphization of the ZnO film.

3.5. Binding energies

Experimental XPS spectra and respective fits were obtained for the Zn 2p doublet, O 1 s singlet, Sb 3d, 4d, and 3p doublets and N 1 s singlet core lines for all samples (Figs. A9-A13). From the analysis of O 1 s and Sb 3d data, there is a strong overlap between these core lines, in particular between the higher binding energy band (C1, see Table 2) from O1s and the Sb $3d_{3/2}$ peak. Hence, additional information was derived from the Sb 4d doublet (with a smaller 5/2 – 3/2 spin-orbit splitting, ~1.2 eV, all samples) and from the Sb 3p doublet (larger spin-orbit split, 45.7 eV, for samples UC and UD). It is evident that as Sb content is increased in ZnO the Sb 3d peaks gradually increase in area with respect to the O1s spectra, whose

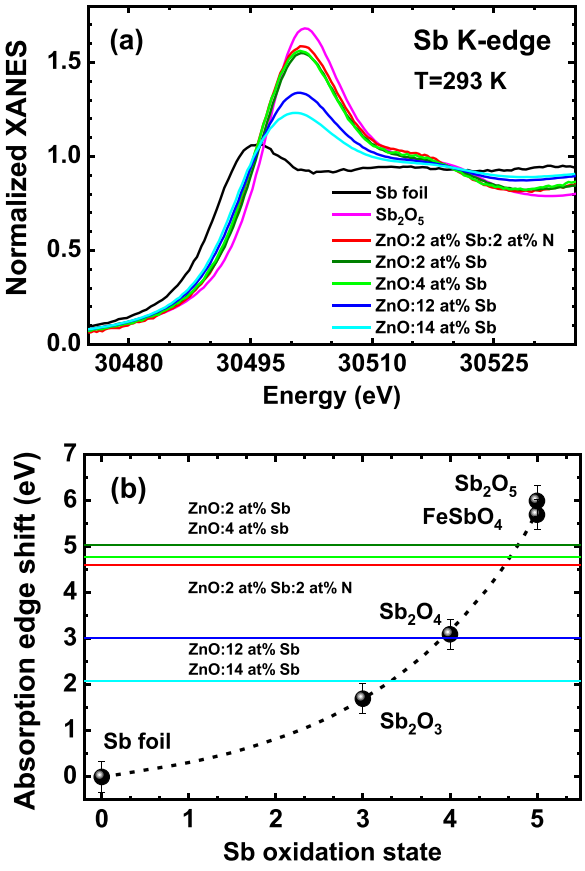


Fig. 7. (a) Sb K-edges XANES spectra for Sb foil, Sb_2O_5 powder, and Sb-doped ZnO thin films at 293 K. (b) The shift of the absorption edge relative to the Sb foil as a function of the antimony oxidation state. The data for Sb_2O_3, Sb_2O_4, and $FeSbO_4$ are from [40]. Horizontal lines correspond to the produced ZnO:xSb thin film samples.

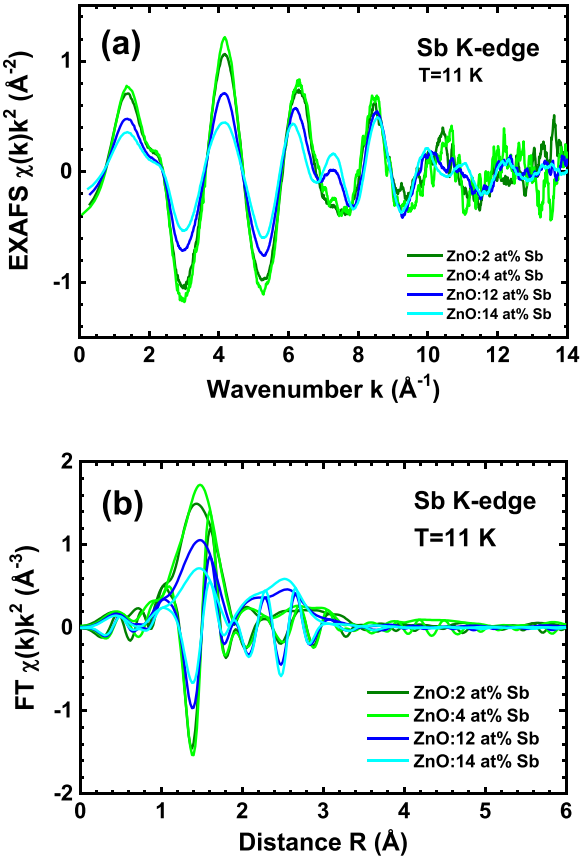


Fig. 8. (a) Experimental Sb K-edges EXAFS $\chi(k)k^2$ spectra and (b) their Fourier transforms (FTs) for Sb-doped ZnO thin films at 11 K.

respective core lines are in the same binding energy range. With the exception of sample UD, all Zn and Sb contributions in other samples are ascribed to the Zn-O and Sb-O bonds. For sample UD, with the highest amount of Sb (14 at%) traces of Sb-Sb metal phases are formed, as seen on both Sb 3d and 4d core lines and discussed in the following paragraphs. The Sb 3d doublet peaks were fitted separately to the O 1 s in order to quantify Sb content independently, with inherent superposition limitations. The strategy consisted in, first, fitting the Sb 3d doublet and, subsequently, fitting the O1s core line and including in it the Sb $3d_{5/2}$ contribution with the same peak position, peak shape, and FWHM. Additionally, the Sb 4d core line was also fit, for comparison with the Sb 3d. For the UD sample with the highest amount of Sb (14 at%), the Sb 3p core line was also fit; hence, for this sample, the Sb content is averaged from these 3 core lines.

In the O 1 s spectra (Figs. A9-A13), contribution C1 (529.8–530.1 eV) alludes to the binding energy of Zn-O and Sb-O bonds, while C2 (531.6–532.0 eV) is ascribed to oxygen/hydroxide or organic impurities on the film surface. Due to the aforementioned superposition of C1 and Sb $3d_{3/2}$ peak, C1 contribution is generally narrower than C2, with FWHM (β_1 and β_2 in Table 2) varying between 1.2 and 1.5 eV and 1.2–1.9 eV and relative areas of 29–57% and 43–71%, respectively. C1 contribution was used to calculate the oxygen atomic concentration listed in Table 2 and decreases with increasing Sb content. Besides oxygen and carbon, the survey spectra are absent of other impurities. Very minute amounts of calcium were found in some samples, albeit not quantifiable. The relative variation of C1 and C2 from O1s is included in Table 2.

The Zn 2p core line (Figs. A9-A13) exhibits two peaks due to spin-orbit splitting (ΔE=23.1 eV, see Table 2), being the most intense (Zn $2p_{5/2}$) fitted (Figs. A9-A13) with a relative area proportion of 1:2 between Zn $2p_{1/2}$ and $2p_{3/2}$ peaks. The latter peak is shifted towards higher binding energies (1021.4–1021.8 eV) as the amount of Sb increases, being the FWHM (β in Table 2) is almost constant (1.7–1.8 eV) for all fits. The position of this peak is attributed to Zn-O bonds [43].

The most studied core line from Sb is the 3d (Figs. A9-A13) [44–47], with a spin-orbit splitting of 9.2 eV (ΔE in Table 2) for all films and a with a relative area proportion of 2:3 between the Sb $3d_{3/2}$ and $3d_{5/2}$ peaks. All films show the main peak of the Sb 3d doublet ($3d_{5/2}$) at 530.3 eV, which is recognized for Sb(III) valence bonds, such as in Sb_2O_3 [44], and in this particular case Sb-O bonds in the ZnO wurtzite cell, as proven by the EXAFS experiments (Section 3.4). For the case of the highest amount of Sb doping (sample UD), an additional doublet is present at lower binding energies (527.3 eV), ascribed to Sb-Sb metallic bonds [44,48,49], with a slightly larger spin-orbit splitting of 9.4 eV and overall 20% contribution. For all films, in order to quantify the atomic oxygen concentration with higher accuracy, the Sb 4d core line was also measured, albeit having a much lower intensity. The position of this line is slightly shifted to higher binding energies (33.9–34.2 eV) with an increase in Sb content; nevertheless, these binding energies are within what is expected for Sb(III), since for Sb(V) the binding energy is slightly greater (~35.5 eV). The spin-orbit splitting in this doublet is very small (~1.2 eV) in comparison to Sb 3d (9.2 eV). The analysis of the latter line for the sample with the highest Sb content (UD, 14 at%) revealed two doublets with $3d_{5/2}$ binding energies of 31.2 eV and 34.2 eV, spin-orbit splitting of 1.1 eV and 1.3 eV, for metallic Sb and Sb(III)-O bonds, respectively. This is indicative that for the highest

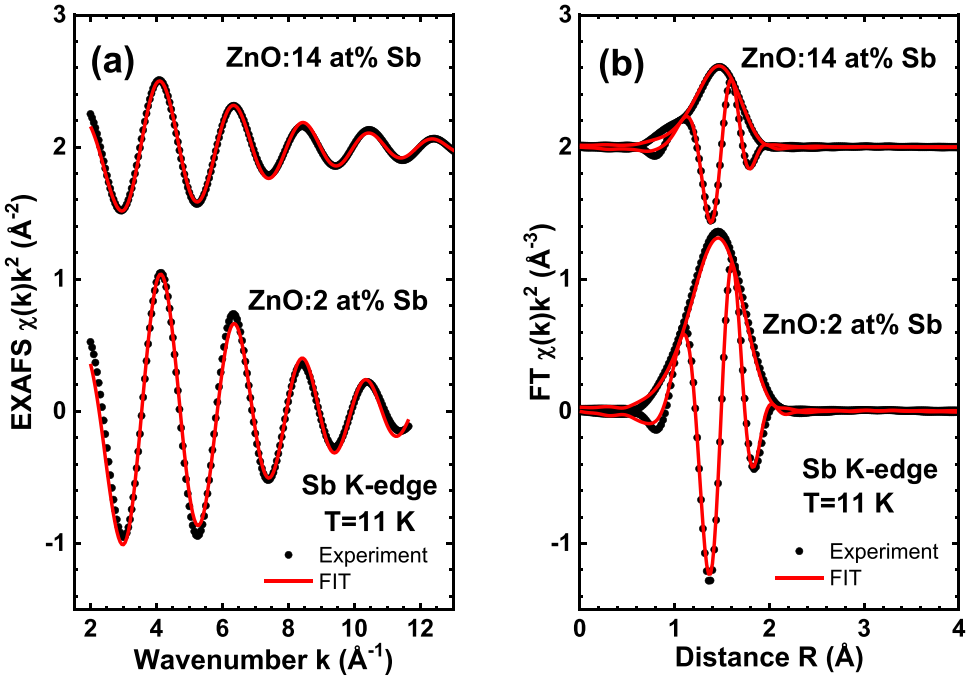


Fig. 9. Best fits of the first-shell experimental Sb K-edges (a) EXAFS $\chi(k)k^2$ spectra and (b) their FTs for Sb-doped (2 and 14 at%) ZnO thin films at 11 K.

Table 2
Composition and core line binding energy positions derived from the XPS fits to the ZnO:Sb films data. ΔE is the spin-orbit separation of the Zn 2p, Sb 3p, Sb 3d and Sb 4d doublets. β is the FWHM of the fitted peaks. A relative area percentage (%) is given for the two O 1 s contributions (C1 and C2) with respective FWHM (β_1 and β_2). The valence band maximum position (VBM) is also shown. For UD, besides the Sb-O 3d doublet at 530.3 eV, an additional 3d doublet is ascribed to Sb-Sb metallic bonds.

Sample	Composition (at%)		Zn 2p	O 1 s	Sb 3d	Sb 4d	Sb 3p	VBM (eV)
			Position / ΔE / β (eV)	C1 (β_1) % C2 (β_2) % (eV)	Position / ΔE / β (eV)	Position / ΔE / β (eV)	Position / ΔE / β (eV)	
UE	Zn	51.9	1021.4	530.1 (1.5)	530.3	33.9	–	2.0 ± 0.1
	O	46.5	23.1	57%	9.2	1.2		
	Sb	1.6	1.8	531.8 (1.2) 43%	1.5	1.2		
UT	Zn	66.5	1021.5	529.9 (1.3)	530.3	34.2	–	2.1 ± 0.1
	O	29.8	23.1	41%	9.2	1.3		
	Sb	1.5	1.8	531.6 (1.8) 59%	1.2	1.1		
	N	2.2						
UF	Zn	56.4	1021.7	530.1 (1.3)	530.3	34.2	–	2.2 ± 0.1
	O	37.8	23.1	45%	9.2	1.2		
	Sb	5.8	1.8	531.8 (1.4) 55%	1.2	1.3		
UC	Zn	48.6	1021.8	529.9 (1.2)	530.3	34.2	768.4	2.3 ± 0.1
	O	39.7	23.1	38%	9.2	1.2	45.7	
	Sb	11.7	1.7	532.0 (1.9) 62%	1.2	1.2	3.6	
UD	Zn	54.2	1021.8	529.8 (1.3)	527.3 (metal 20%)/ 530.3 (oxide	31.2/34.2	768.0	2.3 ± 0.1
	O	32.4	23.1	29%	80%)	1.1/1.3	45.7	
	Sb	13.4	1.7	531.9 (1.3) 71%	9.4/9.2 1.1/1.3	1.1/1.1	4.8	

level of Sb doping there is apparent segregation of Sb atoms to the surface, where XPS is very sensitive. For both Sb 3d and Sb 4d core lines the FWHM (β) is relatively constant (1.1–1.3 eV). An additional core line was measured for Sb, the 3p doublet at 768.0–768.4 eV, with much lower intensity than the Sb 3d and 4d lines, but with a much larger doublet splitting (45.7 eV).

Contrary to the EXAFS analyses for the bulk of the ZnO:Sb films (see last section, 3.4), no other antimony species contributions corresponding to Sb(IV) or Sb(V) valence states were registered. If existing, the latter species should be present at slightly higher binding energies. This indicates that, within the XPS probing depth, the Sb-O bonds have a pyramidal coordination geometry. Whereas, in the bulk, depending on Sb content, this pyramidal coordination is apparent for higher Sb doping (12–14 at%), as opposed to octahedral coordinated Sb(V) valence for lower Sb doping in the bulk, as seen in Section 3.5.

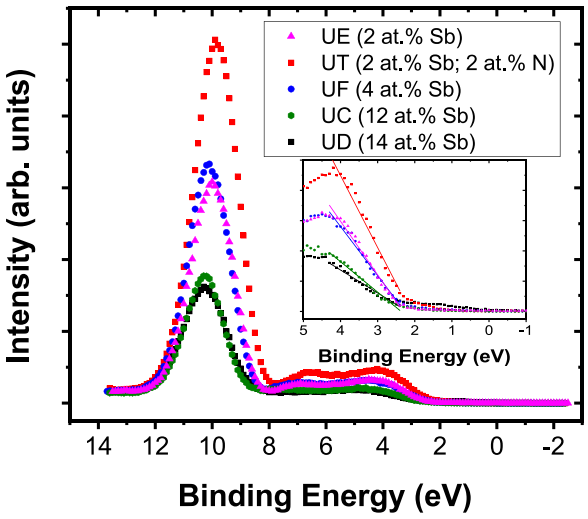


Fig. 10. Valence band edge energy spectra for the ZnO:Sb films. The inset shows enlarged spectra for the determination of VBM.

The relative ratio of the areas of the Sb 3d3/2 and Zn 2p3/2 main doublet peaks as a function of Sb doping in ZnO was calculated and plotted (Fig. A14), where there is an almost linear increase of this ratio from 0.05 to 0.44 in the range of 2 – 12 at% of Sb. For the highest level of Sb doping (14 at%) the ratio is only slightly reduced to 0.43.

The ZnO density of states below the Fermi energy level (E_F, 0 eV) is primarily composed of three bands (Fig. 10): at ~10 eV, ~4 eV, and ~7 eV, ascribed to Zn 3d orbitals, O 2p orbitals and hybridization between both, respectively [50]. The position of the band ascribed to the 3d orbitals increases from approximately 9.8 eV to 10.3 eV with the increase in Sb doping. Competing $Zn_xSb_yO_z$ phases that are developed for higher Sb-doping may be responsible for this shift, as seen from the XRD data (Fig. 2) and STEM micrographs (Fig. 3). The offset of the valence band energy maximum (VBM) relative to the Fermi level was determined from the points of the intercepts of the binding energy linear fits with the background (inset of Fig. 10). VBM increases gradually from ~2.0 eV to ~2.3 eV (shifts downwards from E_F) with the increase in Sb-doping ZnO (Table 2), which is indicative of p-type conducting in the outermost atomic layers of the films.

When analysing the atomic composition data from the RBS and XPS experiments (Table 3), approximate values for Zn, O, and Sb content in all films is obtained by both techniques. However, for sample UT (also doped with N) there is a big discrepancy in Zn and O content by both techniques. RBS requires an input density in the simulation, which may deviate from the bulk/standard values; however, it is very sensitive to in-depth atomic concentration changes. XPS is a surface-sensitive method and provides information from the first 7–10 nm (outermost atomic layers). For the higher Sb-doped ZnO films, the XPS value for the atomic concentration of zinc is larger than that determined by RBS, due to the decreased oxygen concentration (39 at%) and formation of oxygen vacancies at the surface, which leads to an increase in electrical conductivity (as seen in Section 3.7).

Table 3
Composition (at%) summary determined from RBS (Section 3.1, total depth) / XPS experiments (outermost atomic layers).

Sample	Atomic composition RBS/XPS (at%)			
	Zn	O	Sb	N
UE	49.7 / 51.9	48.1 / 46.5	2.2 / 1.6	–
UT	42.5 / 66.5	53.3 / 29.8	2.2 / 1.5	< 2 / 2.2
UF	46.1 / 56.4	50.4 / 37.8	3.5 / 5.8	–
UC	48.0 / 48.6	40.1 / 39.7	11.9 / 11.7	–
UD	46.7 / 54.2	39.0 / 32.4	14.3 / 13.4	–

Table 4
The relative content of Sb in the samples, obtained by dynamic ToF-SIMS.

Sample	Signal ratio (Sb^+/Zn^+) from dynamic ToF-SIMS	Dynamic ToF-SIMS Rel. (SbO/ZnO^-)/10
UE	2	2
UT	1	1
UF	3	3
UC	10	9
UD	11	10

3.6. Time-of-flight secondary ion mass spectrometry

Table 4 shows the Sb^+/Zn^+ (in positive polarity) and SbO^-/ZnO^- (in negative polarity) signal ratios determined by dynamic ToF-SIMS analysis of the whole film layer.

The SIMS data follow semi-quantitatively the Sb/Zn ratio determined by RBS (see Table 1), although for samples with larger antimony contents there is an underestimation of Sb SIMS signals. This is due to the SIMS matrix effect, i.e. the change of ionization probability of sputtered antimony in dependence on co-sputtered matrix components. This matrix effect becomes more pronounced if larger variations in the sample matrix composition are studied. Therefore, the intensity/concentration correlation becomes non-linear. A study on Mg/Gd alloys [51] ranging from 2 to 10 wt% (0.3–1.7 at%) of Gd in Mg showed good linearity of SIMS signals, due to a wider concentration range and different chemistry. The SIMS matrix effect was found to be more pronounced in the current study.

Fig. 11 shows the most important signals from SIMS depth profiles. There is a good coherence between positive and negative polarity analysis recorded from different craters on each sample. From both negative and positive measurements, the material layers and interfaces are clearly discerned, and Sb is present inside the ZnO layer. Remarkably, the width of the interface of the ZnO layer to the underlying silicon differs among the samples. Since mass spectra are recorded from a $300 \times 300\ \mu m^2$ field of view, the definition of the interface is mainly dependent on the roughness of the top layer. All samples are homogeneous in the axes parallel to the substrate but Sb is not always homogeneously distributed throughout the depth of the sample (perpendicular to the substrate) and shows some interesting behaviour, especially in sample UD (14 at% of Sb). Sample UT (2 at% of Sb and 2 at% of N) and UC (12 at% of Sb) show a constant Sb/SbO signal in the films. Contrariwise, sample UE (2 at% of Sb) shows the highest variation in Sb content throughout the film, with higher Sb/SbO signals closer to the substrate. Sample UF (4 at% of Sb) also shows a clear increase in the Sb content near the film/substrate interface. This is similar to what was also discerned by RBS and can relate to diffusion. Interestingly, the Sb signal in negative polarity does not completely match those of SbO, as it is seen a higher Sb signal near the surface of the film. In sample UT, N is not detectable in positive polarity, while in negative polarity the NO/NO_2 signals seem to be constant throughout the film. The higher NO/NO_2 signals in negative polarity near the surface of the film possibly relate to diffusion.

3.7. Optical properties

Through the measurement of the optical transmittance (T) and reflectance (R) of the films, it was possible to calculate the respective optical semiconductor band-gap. An example of the transmittance and reflectance spectra for sample UC (12 at% of Sb doping) is potted in Fig. A15 a). By using equation 1, the absorption coefficient (α) was calculated using the sample thickness (d) and R and T as a function of wavelength:

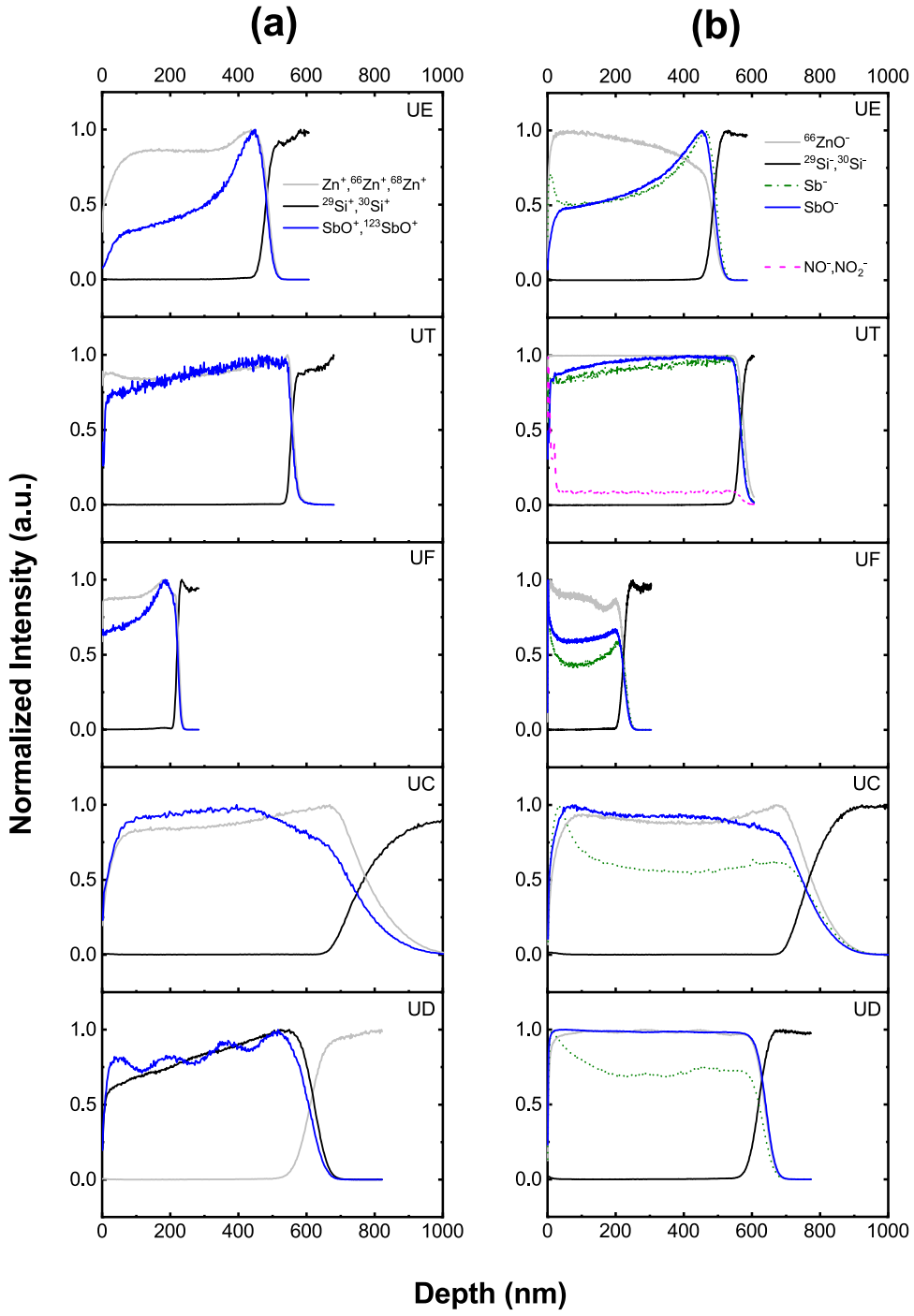


Fig. 11. ToF-SIMS depth profile normalized to maximum signal intensities. In order to achieve good signal dynamics, summations were performed and saturated signals like $^{28}Si^+$ excluded. (a) positive polarity, Zn signal (grey) is a linear combination of Zn^+, $^{66}Zn^+$, and $^{68}Zn^+$ ions, Si signal (black) is a linear combination of $^{29}Si^+$ and $^{30}Si^+$ ions and SbO signal (blue) is a linear combination of $^{121}SbO^+$ and $^{123}SbO^+$ ions; (b) negative polarity, Si signal is a linear combination of $^{29}Si^-$ and $^{30}Si^-$ ions, and NO (pink) signal is a linear combination of NO^- and NO_2^- ions. Note that NO_x^- signals arising during the SIMS process are due to the nitrogen content of UT.

$$\alpha = \frac{1}{d}\ln\left(\frac{1-T}{T}\right) \quad (1)$$

$$(\alpha E)^n = A(h\nu - E_g) \quad (2)$$

where A is a parameter independent of the photon energy $h\nu$ (h is Planck's constant; ν is photon frequency). Subsequently, for the Tauc plots (Fig. A15 b)), $(\alpha E)^n$ was plotted as a function of the photon energy, where $n = 2$ for direct band-gap transitions. With this information it was possible to estimate the band-gap by the Tauc method through the graphical representation of equation 2 and the determination of the intersection of the tangent line to the maximum of this function with the photon energy axis, using confidence bands with a level of 95% of prediction.

Table 5 lists the optical band-gaps of the produced films with respective errors estimated from linear regression statistics. The films with the lower amount of Sb doping have larger band-gaps, in the range of 2.9 – 3.2 eV, while the partially amorphous films with

Table 5
Optical band-gap values for the produced ZnO:Sb films.

Specification		Sb content (at%)	Band-gap [eV]
UE	ZnO:Sb	2	2.90 ± 0.01
UT	ZnO:Sb:N	2	2.88 ± 0.01
UF	ZnO:Sb	4	3.16 ± 0.01
UC	ZnO:Sb	12	2.10 ± 0.01
UD	ZnO:Sb	14	1.60 ± 0.01

Table 6
Seebeck coefficient results for the as-deposited and thermal-treated ZnO:Sb thin films.

Specification		Sb content (at%)	Seebeck Coefficient [μV/K]	
			As-deposited	Thermal-treated
UE	ZnO:Sb	2	-9.3 ± 0.1	-40.3 ± 0.6
UT	ZnO:Sb:N	2	-5.3 ± 0.1	-2.3 ± 0.1
UF	ZnO:Sb	4	-6.1 ± 0.9	-36.3 ± 0.2
UC	ZnO:Sb	12	-18.8 ± 0.4	-55.6 ± 0.8
UD	ZnO:Sb	14	-1.4 ± 0.2	-24.6 ± 0.2

higher Sb content have smaller band-gaps in the range of 1.6–2.1 eV. These values are much smaller than for undoped ZnO (~3.3 eV) [52,53], and for ZnO:Ga and ZnO:Al (~3.4–3.5 eV) [18], enabling the offset absorption of more visible light for ZnO:Sb thin films.

3.8. Thermoelectric property

Seebeck coefficient assessment experiments were performed in a high vacuum. As an example, Fig. A16 shows the experimental data of the UC sample (Sb 12 at%) before and after the post-deposition thermal treatment (TT) in a vacuum furnace at 300 °C for 1 h at a pressure of 10^{-3} Pa. The Seebeck coefficient is taken from the slope of the straight line formed by the experimental data. To calculate the experimental error of the Seebeck coefficient, the linear correlation coefficient is used, which indicates the degree of adjustment of the experimental data to the line. This thus allows the calculation of the slope uncertainty by Eq. (3).

$$\Delta S = a\sqrt{\frac{r^{-2}-1}{N-2}} \tag{3}$$

Where a is the slope, r is the correlation coefficient, and N is the number of measurements. The Seebeck coefficient values for the produced ZnO:Sb thin films for as-deposited and thermal-treated films are presented in Table 6. All values are negative, indicative of n-type carriers. As can be seen, only sample UT (ZnO:Sb:N) did not increase substantially its Seebeck coefficient after thermal treatment, possibly due to the induced disorder from N and Sb doping. If one considers the TT samples, the absolute Seebeck values are almost the same (~40 μV/K) for 2–4 at% of Sb. Further Sb-doping to 12 at% increases this property to a maximum of 56 μV/K. After this threshold, it decreases to 25 μV/K for the subsequent increase in Sb doping to 14 at%, possibly due to the excessive Sb content and inherent induced structural disorder, and enhanced amorphization. The Seebeck coefficient for undoped ZnO is approximately − 2 μV/K.

Table 7 presents the results of the electrical characterization for each sample after heat treatment. From the XRD analysis in Section 3.2, samples UC and UD, those with greater Sb content, were revealed to be partially amorphous due to the distortion introduced by Sb atoms. Because of this, the as-deposited UC and UD films are very resistive (> 100 Ω·cm), and the electrical properties could not be evaluated due to the limitations of our equipment. However, upon annealing, the recrystallization kinetics increased the carrier concentration to ~10^{26} m^{-3} for sample UD and its electrical conductivity to 541 ± 2 $\Omega^{-1}\cdot m^{-1}$, being the highest measured for these films, one order of magnitude larger than for the sample with 12 at% Sb. Most of the films exhibit n- and p-type electrical conductivity. Depending on where the probes are set on the 10 mm × 10 mm square test area on the surface of the film, both types of conduction are registered; more than 10 measurements were performed for each sample, rotating it 90º after each reading. Since the electrical conductivity and respective charge carrier concentration is obtained from the bulk of the film, it surveys crystalline domains with either n- or p-type nature. However, as seen from the valence band edge energy spectra (Fig. 10), and its discussion in the XPS experiments, the VBM increases with Sb doping in ZnO, shifting downwards from the Fermi level, indicating a p-type conductivity in the outermost atomic layers. Prior to electrical conductivity experiments, two standard samples (GaN, In_2O_3:SnO_2) with known electrical conductivity and conductivity type were measured and verified. Samples with smaller Sb content (2 at%) have a carrier concentration of the order of ~10^{22} m^{-3}, which is 4 orders of magnitude smaller than for the highest level of doping (14 at%); the carrier concentration for undoped ZnO is ~10^{21} m^{-3}. This indicates that, despite the decrease in crystallinity (see Fig. 2), and despite the increase in structural disorder apparent from the EXAFS spectra of the Zn K-edge (see Fig. 5), the transition from a Sb^{5+} to Sb^{3+} (as seen in Fig. 7b) with increase in Sb-doping enhances the electrical conductivity and the Seebeck coefficient.

Table 7
Electric and thermoelectric properties of the thermal-treated ZnO:Sb thin films.

Specification		Sb content (at%)	Electrical conductivity ($\Omega^{-1}\cdot m^{-1}$)	Power factor ($\mu W\cdot K^{-2}\cdot m^{-1}$)
UE	ZnO:Sb	2	1.9 ± 0.3	(3 ± 1)× 10^{-3}
UT	ZnO:Sb:N	2	8 ± 2	(4 ± 1)× 10^{-5}
UF	ZnO:Sb	4	72 ± 3	0.10 ± 0.01
UC	ZnO:Sb	12	48 ± 1	0.15 ± 0.01
UD	ZnO:Sb	14	541 ± 2	0.33 ± 0.01

By associating thermoelectric properties and electrical properties, the thermoelectric power factor can be calculated, which is a very important characteristic in the performance classification of a thermoelectric material. The power factor is calculated by Eq. (4), using the Seebeck coefficient (S) and the electrical conductivity (σ).

$$PF = S^2\sigma \tag{4}$$

From Table 7 it can be observed that the sample with the highest power factor is UD (14 at% Sb), 0.33 $\mu W\cdot K^{-2}\cdot m^{-1}$. UC, with 12 at% Sb, has the largest absolute Seebeck coefficient, 56 μV/K and half of the PF of UD, 0.15 $\mu W\cdot K^{-2}\cdot m^{-1}$. Samples with 2–4 at% Sb have an absolute Seebeck coefficient of ~40 μV/K (Table 6) and much smaller power factors (0.003–0.1 $\mu W\cdot K^{-2}\cdot m^{-1}$). Sample UT with N doping has the lowest S and PF, being the intentional N-doping without thermoelectric effect.

4. Conclusions

Transparent thermoelectric ZnO:Sb thin films were deposited by magnetron sputtering, with Sb content varying between 2 and 14 at %. For larger levels of Sb-doping (12–14 at%), the film microstructure is partially amorphous due to the short-range crystalline order (~3 nm), as evidenced by XRD and STEM. Albeit this, the films crystallize in the ZnO wurtzite structure for smaller levels of Sb-doping (2–4 at%).

Temperature-dependent (10–300 K) X-ray absorption spectroscopy study of ZnO:*x*Sb (x = 2–14 at%) thin films was performed at the Zn and Sb K-edges to shed light on the influence of Sb doping on the local atomic structure and disorder in thermoelectric ZnO:Sb thin films. The analysis of the Zn K-edge EXAFS spectra by the reverse Monte Carlo method allowed us to extract detailed and accurate structural information in terms of the radial and bond angle distribution functions. The obtained results suggest that the introduction of antimony to the ZnO matrix promotes static disorder, which leads to the thin film amorphization for large (12–14 at%) Sb content. To adopt such a disordered structure, an increase in the variation of the bonding angle from 4° to 10° between adjacent [ZnO_4] tetrahedra connected by corners and the large values of the Zn–O MSRD, indicating distortions of [ZnO_4] tetrahedra, are required.

The analysis of the Sb K-edge shift provides information on the oxidation state of Sb ions, which is equal to about 3 + in ZnO:14 at% Sb, increases to about 4 + in ZnO:12 at%Sb, and finally becomes close to about 5 + in the samples with low (2–4 at%) Sb content. These results correlate well with the analysis of EXAFS. The local coordination of Sb ions in the ZnO:2–4 at% Sb thin films is about 5–6 oxygen atoms being close to that in Sb_2O_5 [41]. Upon increasing Sb content to 12–14 at%, the coordination and oxidation state of antimony are reduced to three oxygen atoms and 3 + , respectively. Such coordination of antimony can be found in $ZnSb_2O_4$ [42], where it also has an oxidation state 3 + . Sb^{3+} ions with low coordination play the role of the network modifier and promote amorphization of the ZnO film.

RBS experiments enabled the determination of the in-depth atomic composition profiles of the films. For all samples, Zn is slightly depleted in the topmost atomic layers. The Sb content is approximately constant in-depth in all films, but an increase at the film/substrate interface is apparent due to diffusion. This diffusion is most noticeable for the sample with 2 at% of doping, where Sb is stable at that composition in the bulk but increases up to ~6 at% towards the film–silicon substrate interface. From electron microscopy observations, the films with lower Sb-content develop a columnar morphology comprising polycrystalline grains that broaden in the direction of the film growth. Contrariwise, and as predicted from the XRD patterns, the films with the highest concentration of antimony grow without a structural order, developing nanocrystalline grains (~3 nm) in a partially amorphous, matrix. From STEM/HAADF cross-sectional micrographs, for the highest level of Sb doping (14 at%), segregation of Zn- and Sb- rich zones are discerned. The phase segregation to the ZnO-rich side is typically closer to the Si substrate. The film composition at the surfaces, as determined by XPS, matches that of the bulk determined by RBS, except for larger Sb-doped ZnO films, where the concentration of oxygen determined by XPS is smaller near the surface, possibly due to the formation of oxygen vacancies that enhances the electrical conductivity. Traces of Sb-Sb metal bonds were found by XPS for the sample with the highest level of Sb-doping. By analysing the binding energies near the valence band edge, the valence band maximum energy position increases gradually from ~2.0 eV to ~2.3 eV (shifts downwards from E_F) with the increase in Sb-doping ZnO, which is indicative of p-type conducting. However, from the electrical characterization results, both n-type and p-type conductivity was registered in the bulk of the films, which can be justified by a preferential p-type conductivity in the outermost atomic layers.

The TOF-SIMS obtained Sb/Zn and SbO/ZnO ratios follow that of the Sb bulk concentration determined by RBS, although the Sb signals were underestimated for larger Sb content due to the SIMS matrix effect. Contrary to what was discerned by RBS, Sb is not always homogeneously distributed throughout the depth of the films, with the sample with 14 at% of Sb doping showing an interesting behaviour. The samples with smaller Sb content (2 and 4 at% of Sb) show larger Sb content closer to the film-substrate interface, which was also observed by RBS and can be due to diffusion.

From the optical transmittance and reflectance curves, it was determined that the films with the lower amount of Sb doping have larger optical band-gaps, in the range of 2.9 – 3.2 eV, while the partially amorphous films with higher Sb content have smaller band-gaps in the range of 1.6–2.1 eV. Albeit being X-ray amorphous, but evidencing short-range crystalline order, the films with 12 at% of Sb have the highest Seebeck coefficient (~56 μV/K) and corresponding thermoelectric power factor of ~0.2 $\mu W \cdot K^{-2} \cdot m^{-1}$. These thermoelectric properties results endows the application of these transparent ZnO:Sb thin films for heat harvesting applications in order to render, for example, touch screens, photovoltaic modules, and other electronic devices, more energetically sustainable.

CRediT authorship contribution statement

Joana M. Ribeiro: Investigation, Writing. **Frederico J. Rodrigues**: Investigation. **Filipe C. Correia**: Investigation. **Inga Pudza**: Investigation. **Alexei Kuzmin**: Investigation, Writing, Software, Conceptualization, Funding acquisition. **Aleksandr Kalinko**: Research, Software. **Edmund Welter**: Resources. **Nuno P. Barradas**: Research, Software. **Eduardo Alves**: Research, Software, Resources. **Alec P. LaGrow**: Research, Resources. **Oleksandr Bondarchuk**: Research. **Alexander Welle**: Research, Software, Resources. **Ahmad Telfah**: Validation, Investigation. **Carlos J. Tavares**: Conceptualization, Validation, Investigation, Software, Resources, Supervision, Funding acquisition.

Data availability

Data will be made available on request.

Declaration of Competing Interest

The authors declare that they have no known competing financial interests or personal relationships that could have appeared to influence the work reported in this paper.

Acknowledgements

The experiment at HASYLAB/DESY was performed within the project I-20200161 EC. The research leading to this result has been supported by the project CALIPSOplus under the Grant Agreement 730872 from the EU Framework Programme for Research and Innovation HORIZON 2020. Institute of Solid State Physics, University of Latvia as the Center of Excellence has received funding from the European Union's Horizon 2020 Framework Programme H2020-WIDESPREAD-01–2016-2017-TeamingPhase2 under grant agreement No. 739508, project CAMART2. This work was carried out in part through the use of the INL Advanced Electron Microscopy, Imaging and Spectroscopy Facility. This work (proposal ID 2018–020-022469) was carried out with the support of the Karlsruhe Nano Micro Facility (KNMFi, www.knmf.kit.edu), a Helmholtz Research Infrastructure at Karlsruhe Institute of Technology (KIT, www.kit.edu). Joana Ribeiro is grateful to the Fundação para a Ciência e Tecnologia (FCT, Portugal) for the Ph.D grant SFRH/BD/147221/2019. Filipe Correia is grateful to the FCT, Portugal, for the Ph.D. grant SFRH/BD/111720/2015. The authors also acknowledge the funding from FCT/PIDDAC through the Strategic Funds project reference UIDB/04650/2020–2023.

Appendix

See Figs. A1–A16 here.

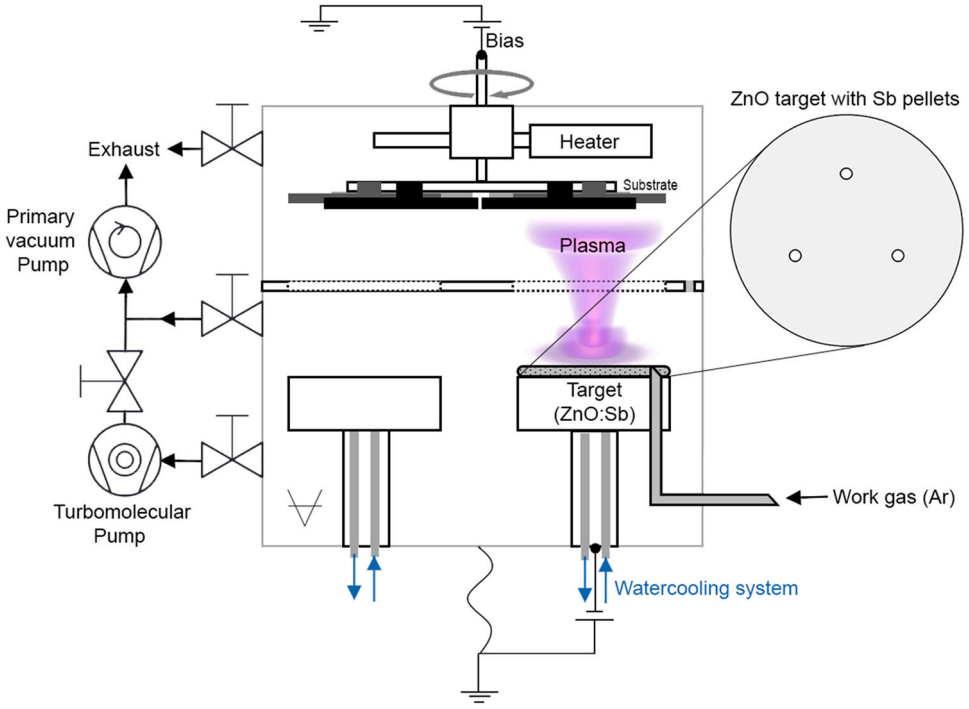


Fig. A1. Schematic of the deposition system for producing the ZnO:Sb films.

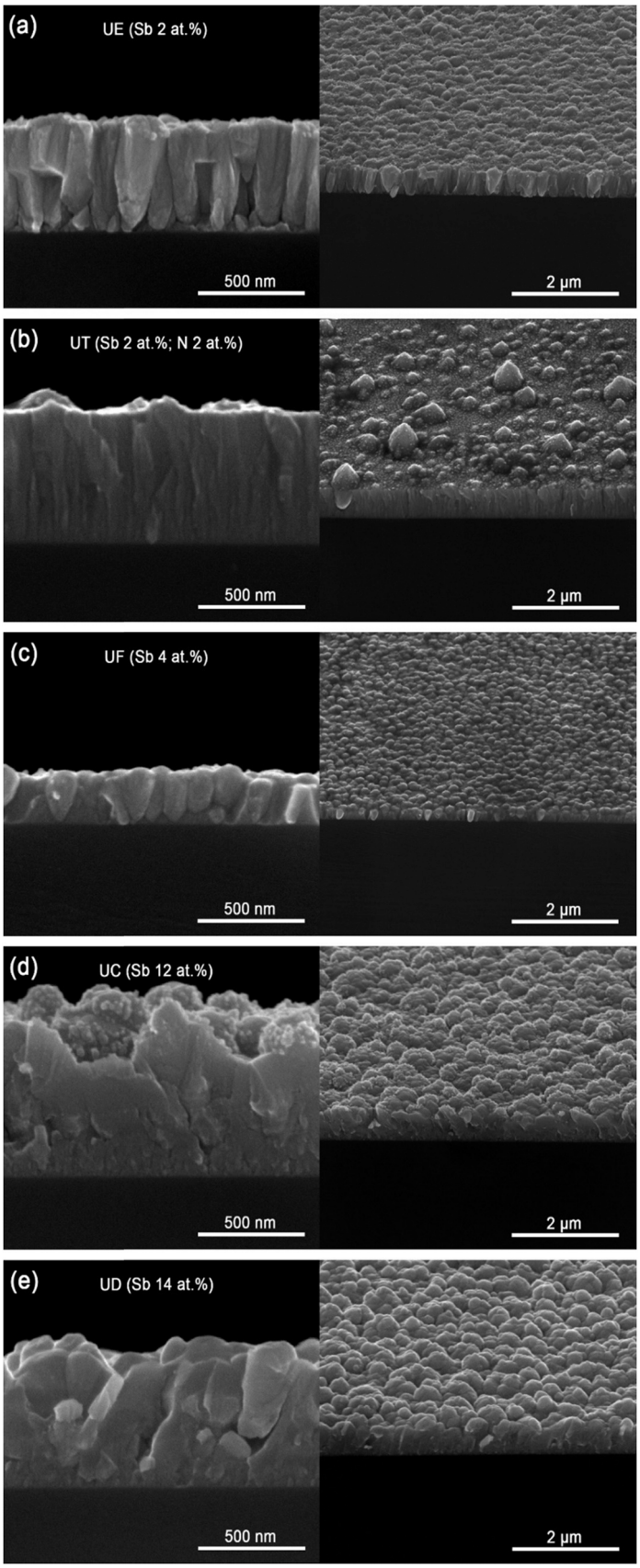


Fig. A2. SEM surface and cross-sectional micrographs for the as-deposited ZnO thin films with varying Sb content.

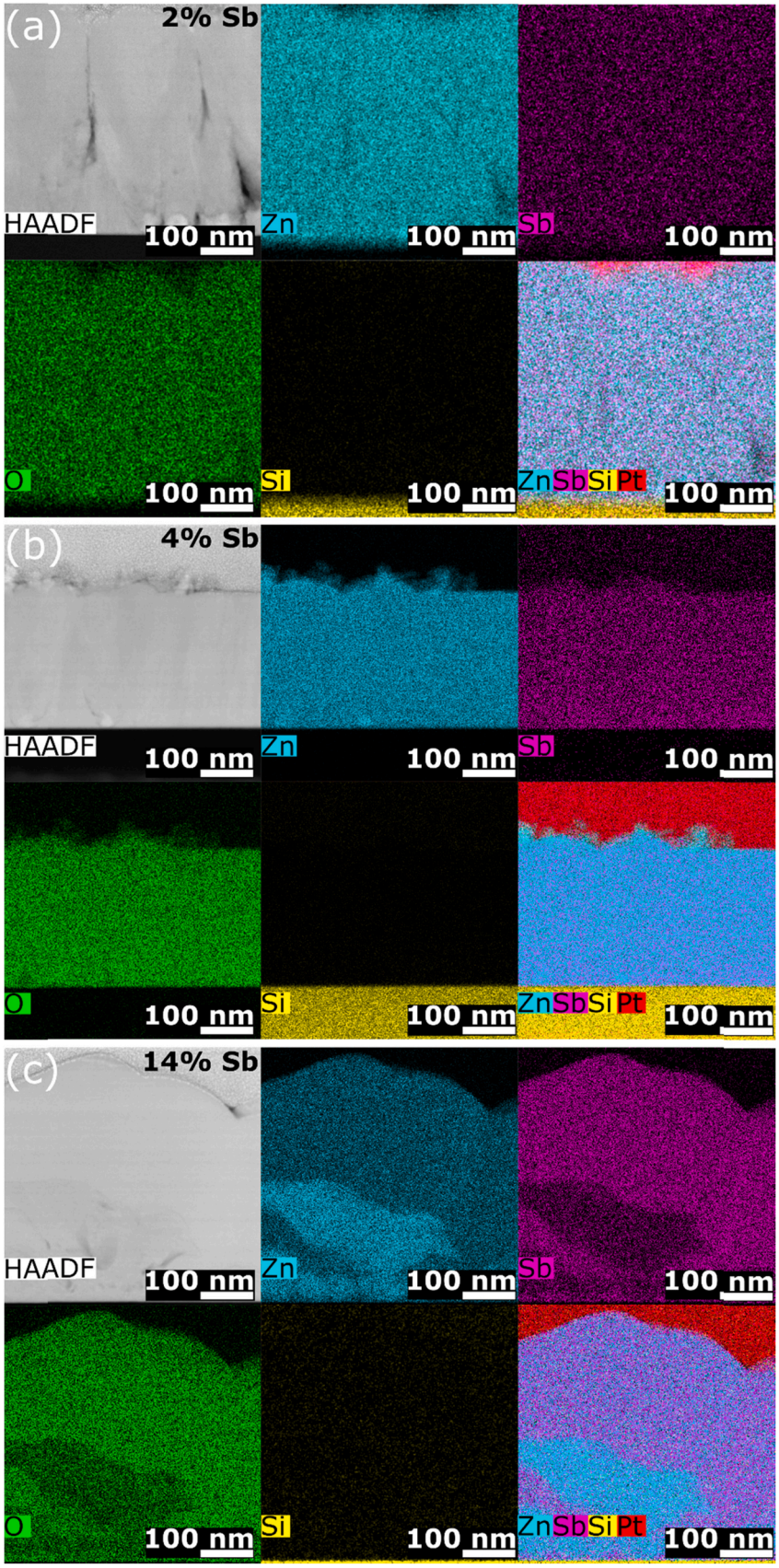


Fig. A3. STEM/HAADF cross-sectional micrographs with chemical element maps for ZnO:Sb films with a) Sb 2 at% (UE), b) Sb 4 at% (UF), and c) Sb 14 at% (UD). Platinum was deposited for the FIB sample preparation process.

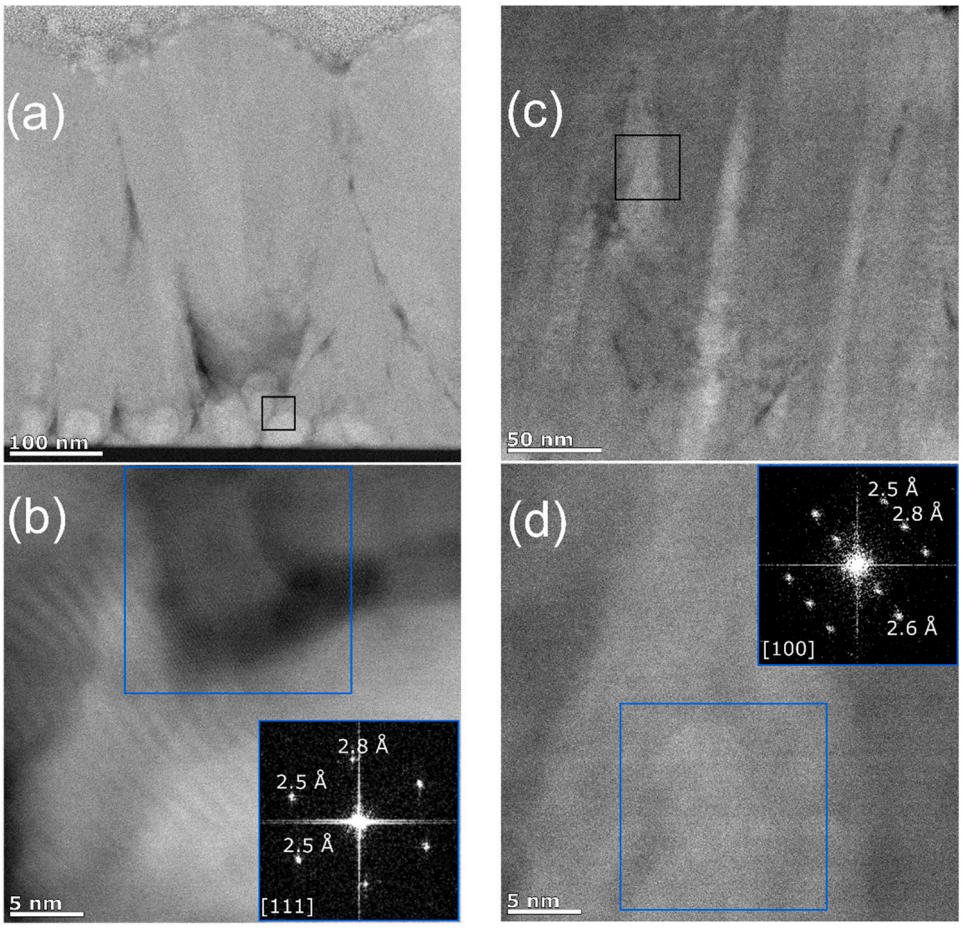


Fig. A4. STEM cross-sectional micrographs with inset FFT of a selected grain (blue square) from sample (a,b) ZnO: Sb 2 at% (UE) and (c,d) ZnO: Sb 4 at% (UF). The blue squares in b) and d) are a magnification of the zone indicated by the black squares in a) and c). The diffraction patterns along b) [111] and d) [100] are representative of the ZnO wurtzite structure.

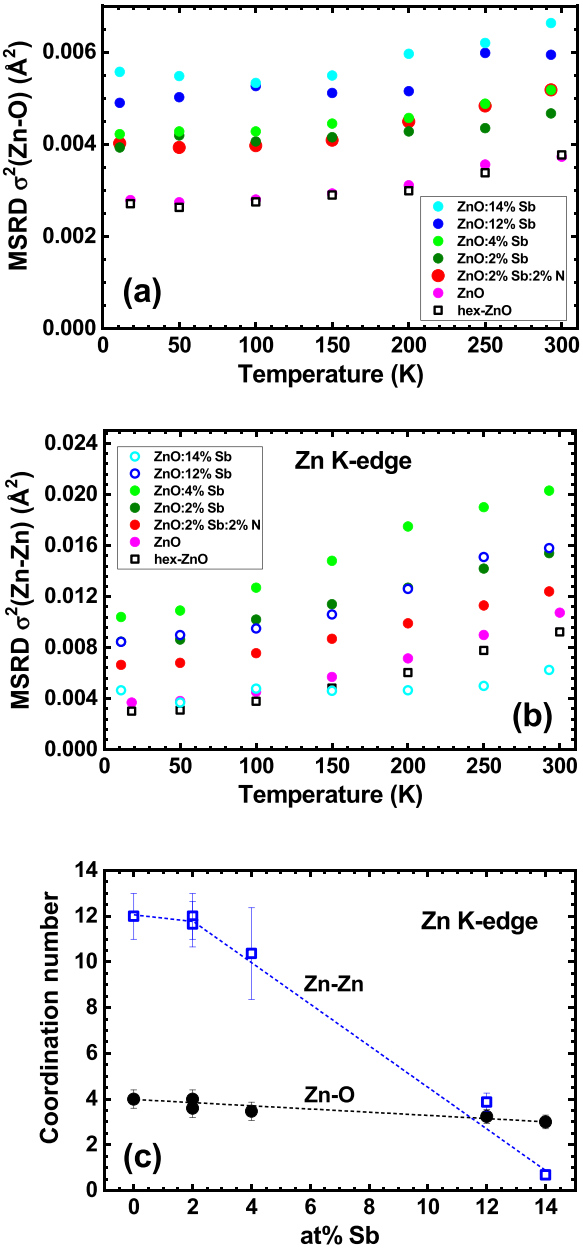


Fig. A5. Temperature-dependence of the mean-square relative displacements (MSRDs) for (a) Zn–O and (b) Zn–Zn atom pairs in the first and second coordination shells of zinc, respectively, for hex-ZnO powder, undoped (ZnO) and Sb-doped ZnO thin films. (c) The composition dependence of the coordination numbers of zinc in the first and second shells for the same samples at 11 K.

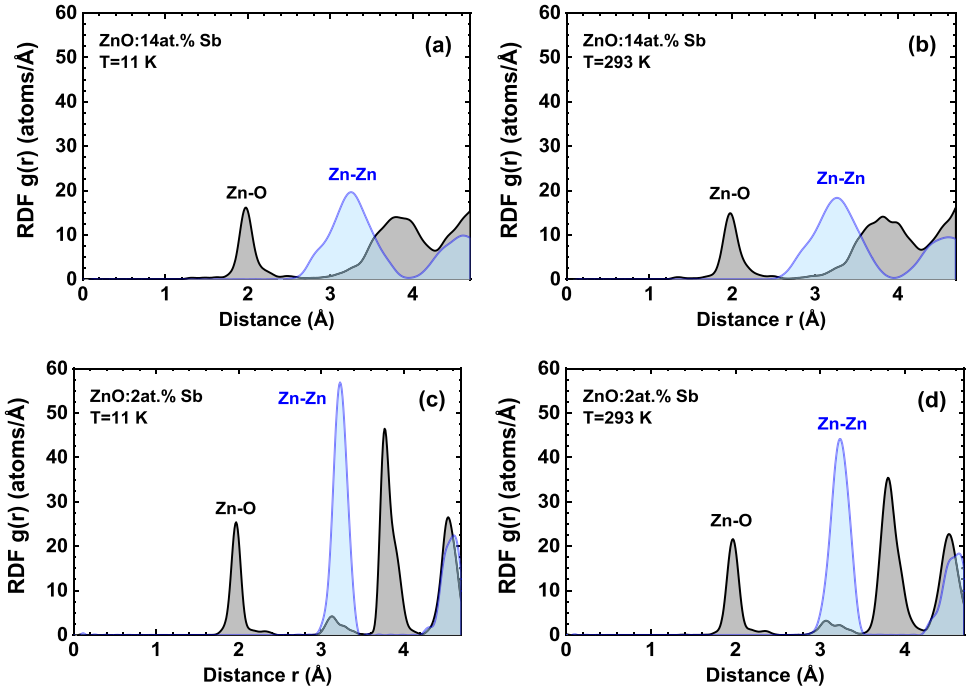


Fig. A6. Radial distribution functions (RDFs) g(r) for Zn–O and Zn–Zn atom pairs obtained by the RMC method from the Zn K-edge EXAFS spectra of ZnO:*x*Sb (*x* = 2 and 14 at%) thin films at 11 and 293 K.

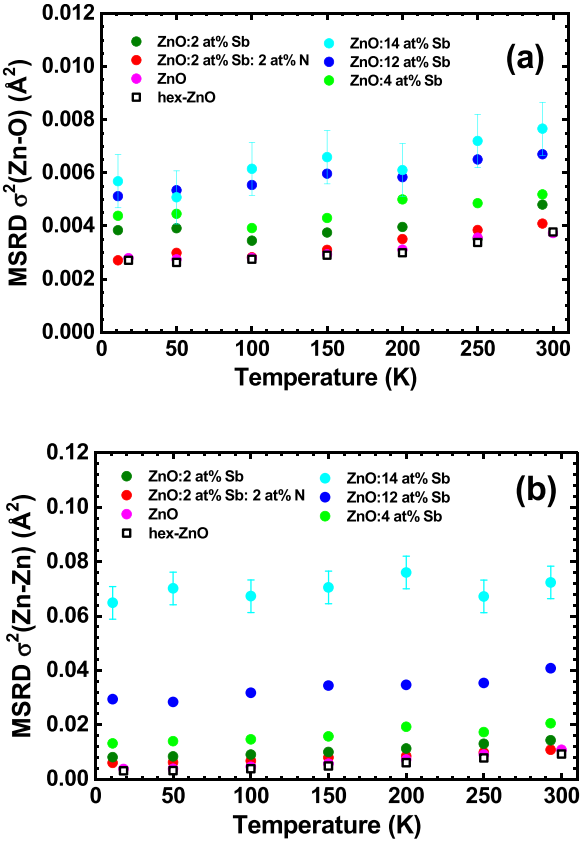


Fig. A7. Temperature-dependence of the mean-square relative displacements (MSRDs) obtained from RMC simulations for (a) Zn–O and (b) Zn–Zn atom pairs in the first and second coordination shells of zinc, respectively, for hex-ZnO powder, undoped (ZnO) and Sb-doped ZnO thin films.

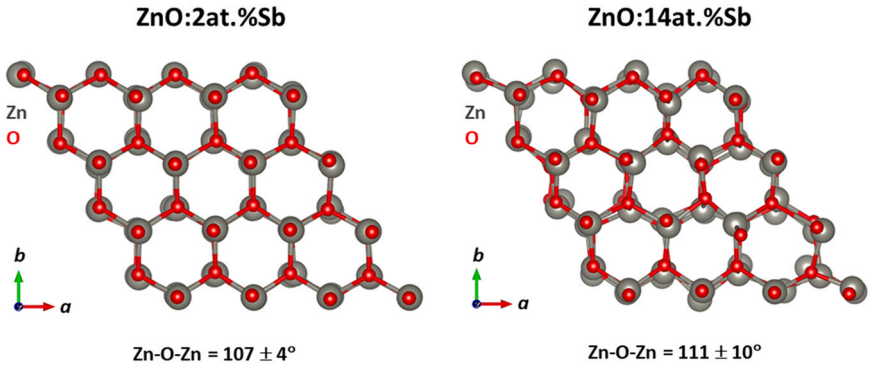


Fig. A8. Atomic configurations from the RMC simulations for ZnO:*x*Sb (*x* = 2 and 14 at%) thin films at 11 K. The values of the average Zn–O–Zn angles are given.

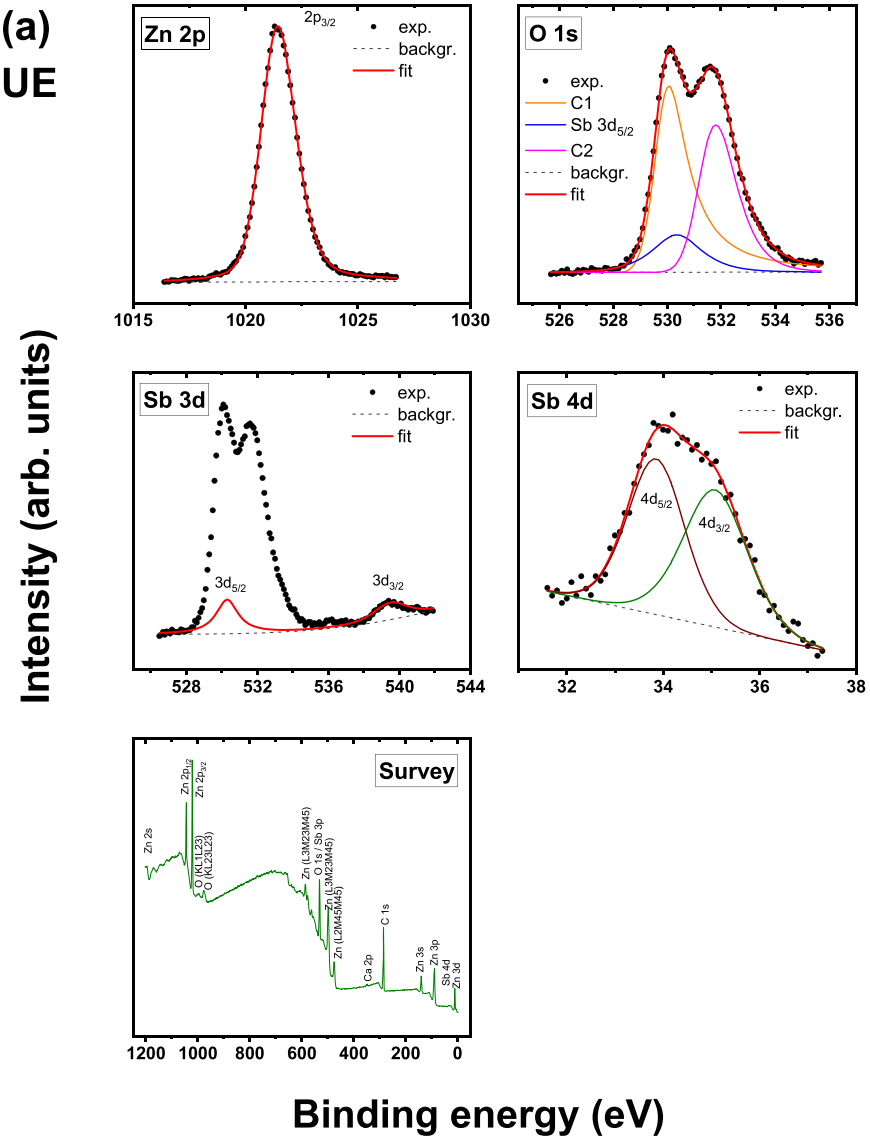


Fig. A9. XPS spectra and respective fits for sample UE (Sb 2 at%): a) Zn 2p, b) O 1 s, c) Sb 3d, d) Sb 4d, e) survey spectra.

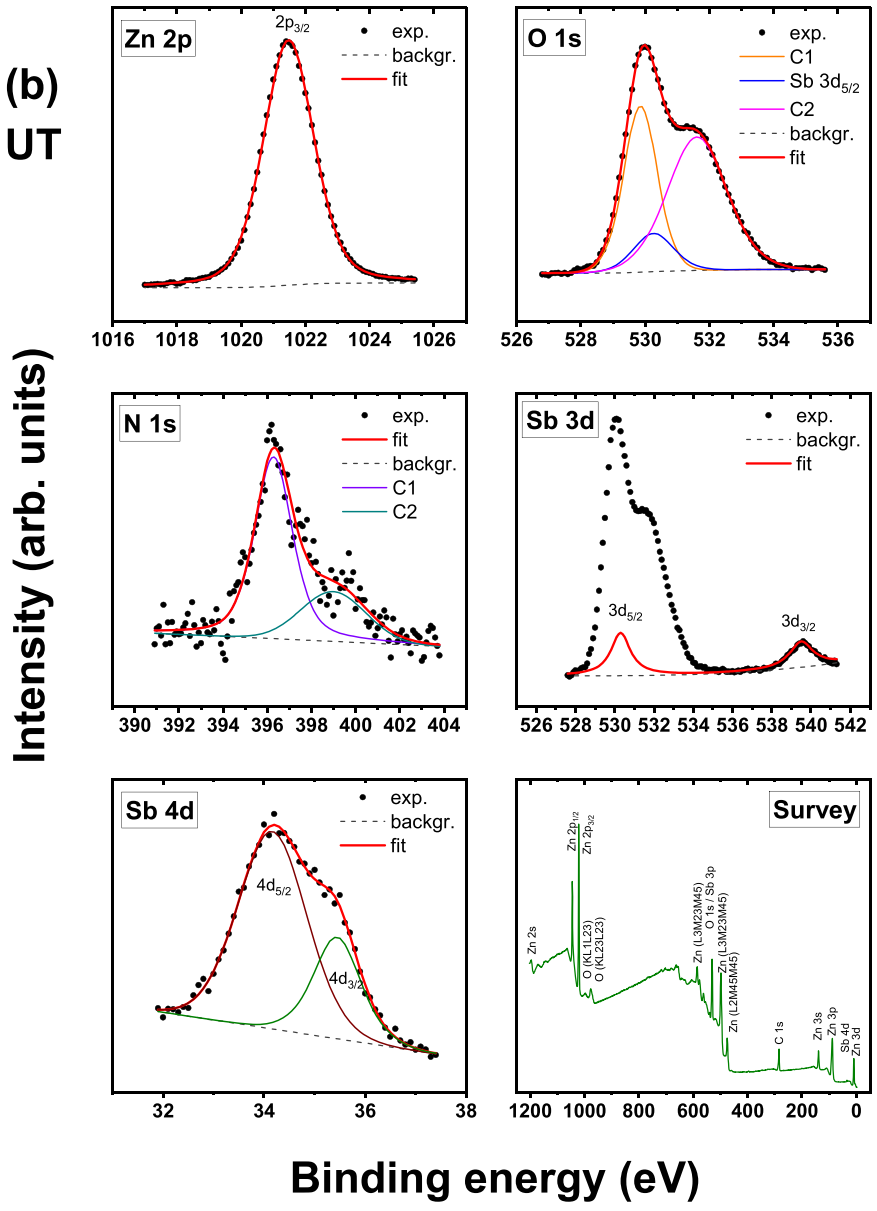


Fig. A10. XPS spectra and respective fits for sample UT (Sb 2 at%; N 2 at%): a) Zn 2p, b) O 1 s, c) Sb 3d, d) Sb 4d, e) N 1 s, f) survey spectra.

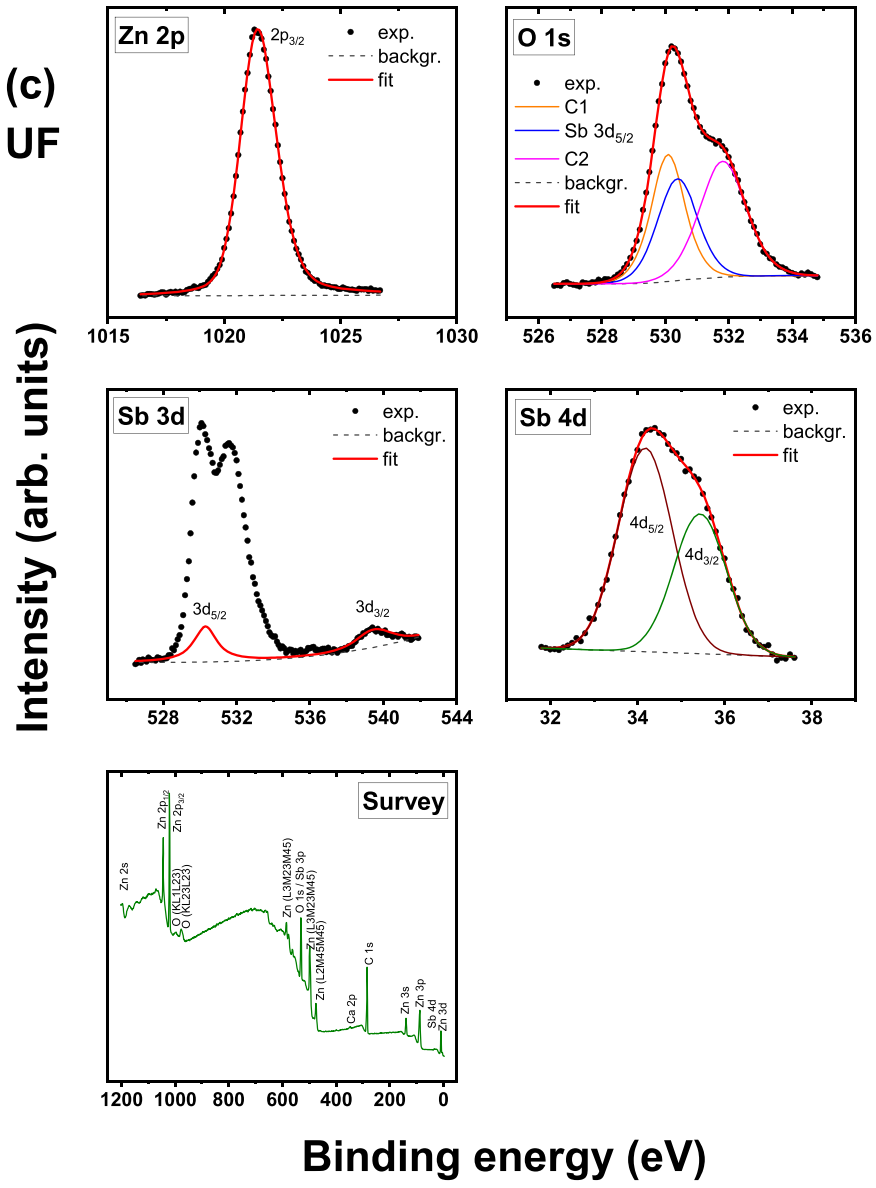


Fig. A11. XPS spectra and respective fits for sample UF (Sb 4 at%): a) Zn 2p, b) O 1 s, c) Sb 3d, d) Sb 4d, e) survey spectra.

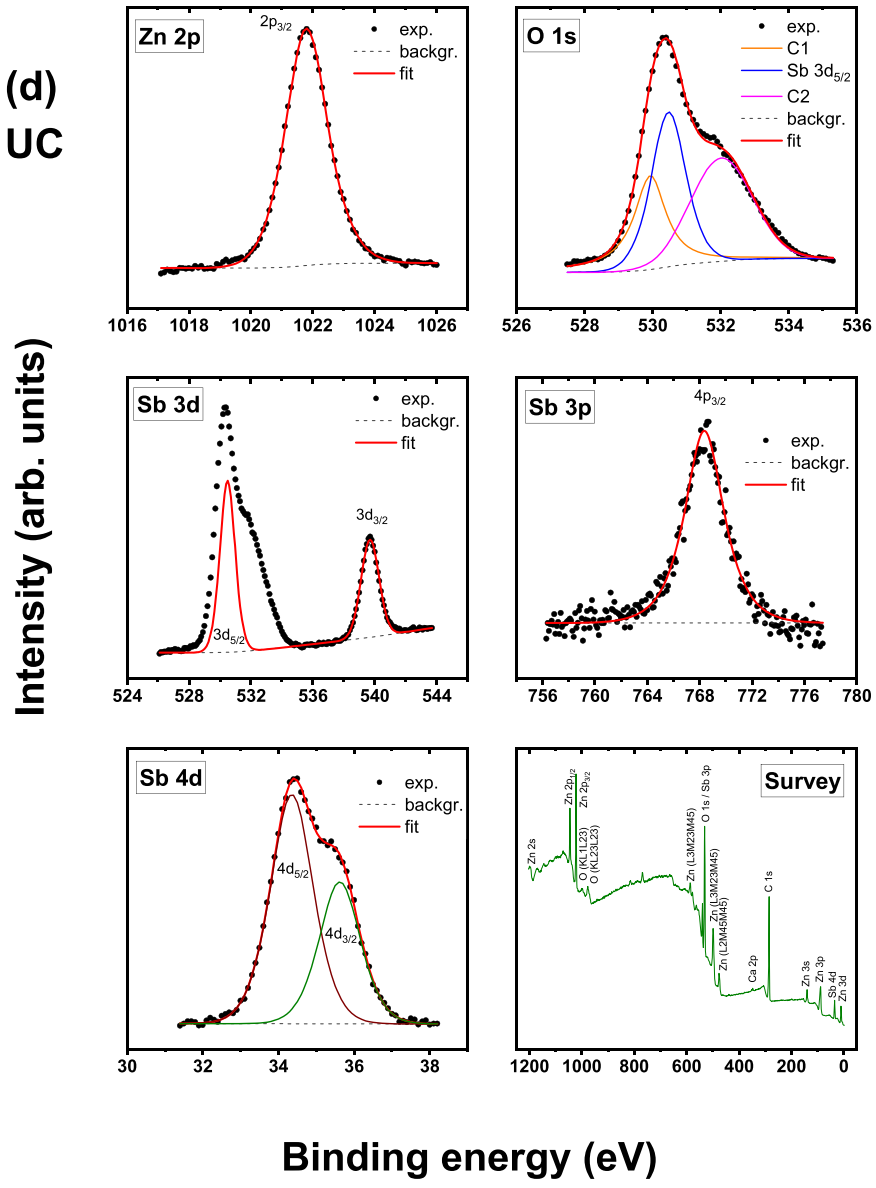


Fig. A12. XPS spectra and respective fits for sample UC (Sb 12 at%): a) Zn 2p, b) O 1 s, c) Sb 3d, d) Sb 4d, e) Sb 3p, f) survey spectra.

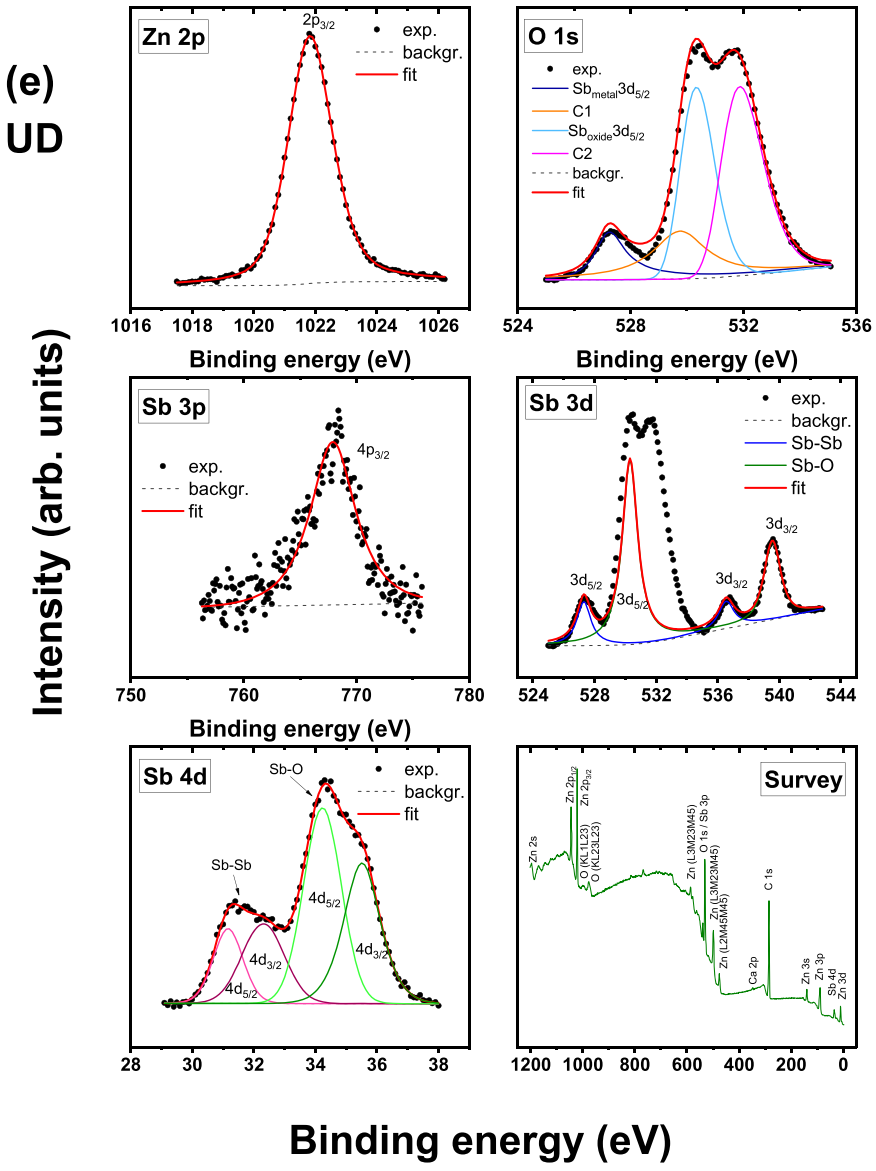


Fig. A13. XPS spectra and respective fits for sample UD (Sb 14 at%): a) Zn 2p, b) O 1 s, c) Sb 3d, d) Sb 4d, e) survey spectra.

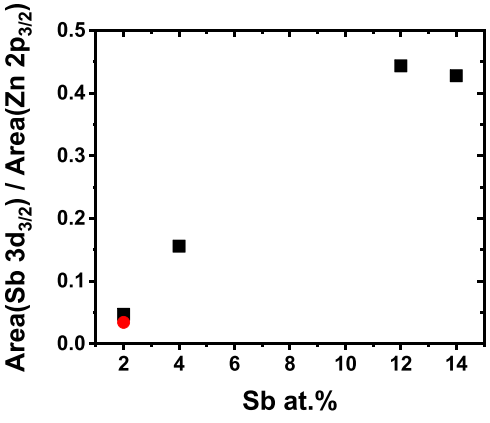


Fig. A14. Relative ratio of the areas of the Sb $3d_{3/2}$ and Zn $2p_{3/2}$ main doublet peaks as a function of Sb doping in ZnO. Square (black) and dot (red) symbols are for ZnO:Sb and ZnO:Sb,N films, respectively.

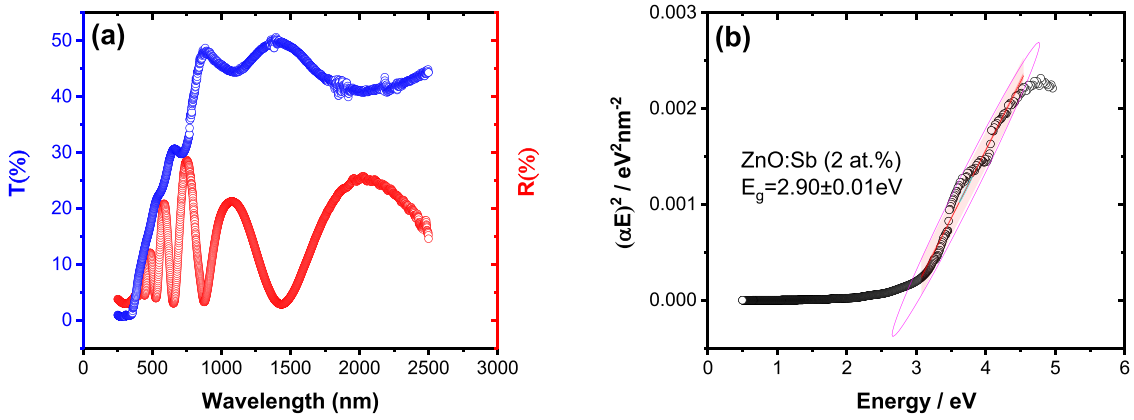


Fig. A15. a) Transmittance and reflectance spectra and respective b) Tauc plot for sample UE (Sb 2 at%).

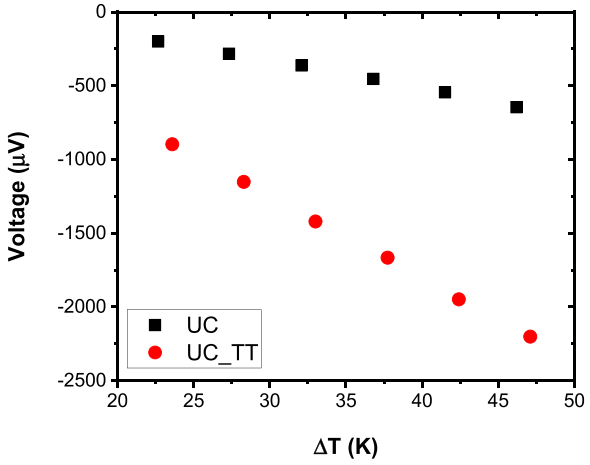


Fig. A16. Evolution of the Seebeck voltage with a varying thermal gradient across the surface of as-deposited (black squares) and thermal-treated (TT; red dots) UC sample (Sb 12 at%).

References

[1] T. Minami, Transparent conducting oxide semiconductors for transparent electrodes, Semicond. Sci. Technol. 20 (2005) S35–S44, https://doi.org/10.1088/0268-1242/20/4/004

[2] H. Hosono, K. Ueda, Transparent conductive oxides, in: S. Kasap, P. Capper (Eds.), Springer Handb. Electron. Photonic Mater. Springer International Publishing, Cham, 2017, p. 1, https://doi.org/10.1007/978-3-319-48933-9_58

[3] P. Jood, R.J. Mehta, Y. Zhang, T. Borca-Tasciuc, S.X. Dou, D.J. Singh, G. Ramanath, Heavy element doping for enhancing thermoelectric properties of nanostructured zinc oxide, RSC Adv 4 (2014), pp. 6363–6368, https://doi.org/10.1039/c3ra46813e

[4] S. Teehan, H. Efstathiadis, P. Haldar, Enhanced power factor of Indium co-doped ZnO:Al thin films deposited by RF sputtering for high temperature thermoelectrics, J. Alloy. Compd. 509 (2011) 1094–1098, https://doi.org/10.1016/j.jallcom.2010.10.004

[5] L. Li, L. Fang, X.M. Chen, J. Liu, F.F. Yang, Q.J. Li, G.B. Liu, S.J. Feng, Influence of oxygen argon ratio on the structural, electrical, optical and thermoelectrical properties of Al-doped ZnO thin films, Phys. E Low-Dimensional Syst. Nanostruct. 41 (2008) 169–174, https://doi.org/10.1016/j.physe.2008.07.001

[6] J.M. Ribeiro, F.C. Correia, P.B. Salvador, L. Rebouta, L.C. Alves, E. Alves, N.P. Barradas, A. Mendes, C.J. Tavares, Compositional analysis by RBS, XPS and EDX of ZnO:Al,Bi and ZnO:Ga,Bi thin films deposited by d.c. magnetron sputtering, Vacuum 161 (2019) 268–275, https://doi.org/10.1016/j.vacuum.2018.12.038

[7] S.-H. Park, J.-Y. Ryu, H.-H. Choi, T.-H. Kwon, Zinc oxide thin film doped with Al2O3, TiO2 and V2O5 as sensitive sensor for trimethylamine gas, Sens. Actuators B Chem. 46 (1998) 75–79, https://doi.org/10.1016/S0925-4005(97)00324-9

[8] N.J. Dayan, S.R. Sainkar, R.N. Karekar, R.C. Aiyer, Formulation and characterization of ZnO:Sb thick-film gas sensors, Thin Solid Films 325 (1998) 254–258, https://doi.org/10.1016/S0040-6090(98)00501-X

[9] M.W. Gaultois, T.D. Sparks, C.K.H. Borg, R. Seshadri, W.D. Bonificio, D.R. Clarke, Data-driven review of thermoelectric materials: Performance and resource considerations, Chem. Mater. 25 (2013) 2911–2920, https://doi.org/10.1021/cm400893e

[10] J. Heremans, M. Dresselhaus, L. Bell, D. Morelli, When thermoelectrics reached the nanoscale, Nat. Nanotechnol. 8 (2013) 471–473, https://doi.org/10.1038/nnano.2013.129

[11] A.M. Rao, X. Ji, T.M. Tritt, Properties of nanostructured one-dimensional and composite thermoelectric materials, MRS Bull. 31 (2011) 218–223, https://doi.org/10.1557/mrs2006.48

[12] A. Krtschil, A. Dadgar, N. Oleynik, J. Bläsing, A. Diez, A. Krost, Local p-type conductivity in zinc oxide dual-doped with nitrogen and arsenic, Appl. Phys. Lett. 87 (2005) 1–3, https://doi.org/10.1063/1.2149171

[13] Y. Yan, J. Li, S. Wei, M. Al-Jassim, Possible approach to overcome the doping asymmetry in wideband gap semiconductors, Phys. Rev. Lett. 98 (2007) 1–4, https://doi.org/10.1103/PhysRevLett.98.135506

[14] P. Jood, R.J. Mehta, Y. Zhang, G. Peleckis, X. Wang, R.W. Siegel, T. Borca-Tasciuc, S.X. Dou, G. Ramanath, Al-doped zinc oxide nanocomposites with enhanced thermoelectric properties, Nano Lett. 11 (2011) 4337–4342, https://doi.org/10.1021/nl202439h

[15] M. Ohtaki, K. Araki, K. Yamamoto, High thermoelectric performance of dually doped ZnO ceramics, J. Electron. Mater. 2009, pp. 1234–1238, https://doi.org/10.1007/s11664-009-0816-1

[16] P. Jood, R.J. Mehta, Y. Zhang, T. Borca-Tasciuc, S.X. Dou, D.J. Singh, G. Ramanath, Heavy element doping for enhancing thermoelectric properties of nanostructured zinc oxide, RSC Adv. 4 (2014) 6363, https://doi.org/10.1039/c3ra46813e

[17] G. Li, X. Lin, S. Liu, B. Jia, Q. Wang, Sb content dependent thermoelectric properties of the p-type ZnO:Sb films fabricated by oxidation method, Appl. Surf. Sci. 439 (2018) 82–87, https://doi.org/10.1016/j.apsusc.2018.01.068

[18] F.C. Correia, P.B. Salvador, J.M. Ribeiro, A. Mendes, C.J. Tavares, Effect on the electrical and morphological properties of Bi incorporation into ZnO:Ga and ZnO:Al thin films deposited by confocal magnetron sputtering, Vacuum 152 (2018) 252–260, https://doi.org/10.1016/j.vacuum.2018.03.033

[19] S.D.N. Luu, T.A. Duong, T.B. Phan, Effect of dopants and nanostructuring on the thermoelectric properties of ZnO materials, Adv. Nat. Sci. Nanosci. Nanotechnol. 10 (2019), https://doi.org/10.1088/2043-6254/ab22ad
[20] X. Liang, Thermoelectric transport properties of naturally nanostructured Ga–ZnO ceramics: Effect of point defect and interfaces, J. Eur. Ceram. Soc. 36 (2016) 1643–1650, https://doi.org/10.1016/j.jeurceramsoc.2016.02.017
[21] Z. Zhou, M. Zou, Y. Xu, J. Lan, C. Liu, A. Ahmad, Y.H. Lin, C.W. Nan, High thermoelectric performance of high-mobility Ga-doped ZnO films via homogenous interface design, J. Am. Ceram. Soc. 104 (2021) 3992–3999, https://doi.org/10.1111/JACE.17789
[22] A.T.T. Pham, O.K.T. Le, T.T.T. Phan, D. Van Hoang, T.H. Nguyen, N.D. Le, T.B. Phan, V.C. Tran, Enhancing transparent thermoelectric properties of Sb-doped ZnO thin films via controlled deposition temperature, Vacuum 202 (2022) 111137, https://doi.org/10.1016/j.vacuum.2022.111137
[23] N.P. Barradas, High depth resolution Rutherford backscattering analysis of Si ± Si 0×78 Ge 0×22 /(0 0 1) Si superlattices, Nucl. Instrum. Methods Phys. Res. 139 (1998) 239–243.
[24] N.P. Barradas, C. Pascual-Izarra, Double scattering in RBS analysis of PtSi thin films on Si, Nucl. Instrum. Methods Phys. Res. Sect. B Beam Interact. Mater. At. 228 (2005) 378–382, https://doi.org/10.1016/J.NIMB.2004.10.074
[25] N.P. Barradas, M.A. Reis, Accurate calculation of pileup effects in PIXE spectra from first principles, X-Ray Spectrom. 35 (2006) 232–237, https://doi.org/10.1002/XRS.903
[26] L.J. van der PAUW, A method of measuring specific resistivity and hall effect of discs of arbitrary shape, Semicond. Devices Pioneer. Pap. WORLD SCIENTIFIC, 1991, pp. 174–182, https://doi.org/10.1142/9789814503464_0017
[27] E. Welter, R. Chernikov, M. Herrmann, R. Nemausat, A beamline for bulk sample x-ray absorption spectroscopy at the high brilliance storage ring PETRA III, AIP Conf. Proc. 2054 (2019) 1–6, https://doi.org/10.1063/1.5084603
[28] A. Kalinko, GitHub - aklnk/xaesa, XAESA v0.05, 2022. ⟨https://github.com/aklnk/xaesa⟩ (accessed May 25, 2022).
[29] A. Kuzmin, J. Chaboy, EXAFS and XANES analysis of oxides at the nanoscale, IUCrJ 1 (2014) 571–589, https://doi.org/10.1107/S2052252514021101
[30] A. Kuzmin, S. Larcheri, F. Rocca, Zn K-edge XANES in nanocrystalline ZnO, J. Phys. Conf. Ser. 93 (2007) 012045, https://doi.org/10.1088/1742-6596/93/1/012045
[31] F.C. Correia, J.M. Ribeiro, A. Kuzmin, I. Pudza, A. Kalinko, E. Welter, A. Mendes, J. Rodrigues, N. Ben Sedrine, T. Monteiro, M.R. Correia, C.J. Tavares, The role of Ga and Bi doping on the local structure of transparent zinc oxide thin films, J. Alloy. Compd. 870 (2021) 159489, https://doi.org/10.1016/j.jallcom.2021.159489
[32] A.L. Ankudinov, B. Ravel, J.J. Rehr, S.D. Conradson, Real-space multiple-scattering calculation and interpretation of x-ray-absorption near-edge structure, Phys. Rev. B. 58 (1998) 7565–7576, https://doi.org/10.1103/PhysRevB.58.7565
[33] J.J. Rehr, R.C. Albers, Theoretical approaches to x-ray absorption fine structure, Rev. Mod. Phys. 72 (2000) 621–654, https://doi.org/10.1103/RevModPhys.72.621
[34] L. Hedin, B.I. Lundqvist, Explicit local exchange-correlation potentials, J. Phys. C. Solid State Phys. 4 (1971) 2064–2083, https://doi.org/10.1088/0022-3719/4/14/022
[35] J. Timoshenko, A. Anspoks, A. Kalinko, A. Kuzmin, Temperature dependence of the local structure and lattice dynamics of wurtzite-type ZnO, Acta Mater. 79 (2014) 194–202, https://doi.org/10.1016/j.actamat.2014.07.029
[36] A. Kuzmin, I. Pudza, K. Klementiev, In situ study of zinc peroxide decomposition to zinc oxide by X-ray absorption spectroscopy and reverse Monte Carlo simulations, Phys. Status Solidi (2022) 2200001, https://doi.org/10.1002/PSSB.202200001
[37] J.M. Ribeiro, F.C. Correia, A. Kuzmin, I. Jonane, M. Kong, A.R. Goñi, J.S. Reparaz, A. Kalinko, E. Welter, C.J. Tavares, Influence of Nb-doping on the local structure and thermoelectric properties of transparent TiO2:Nb thin films, J. Alloy. Compd. 838 (2020) 155561, https://doi.org/10.1016/j.jallcom.2020.155561
[38] U. Betke, Missing Piece in the Crystal Chemistry of Zn-Sb Secondary Phases in ZnO-Sb2O3-Bi2O3Varistor Ceramics: Orthorhombic β-Zn7Sb2O12. An Experimental and Theoretical Study of the Crystal Structure and Its Thermal and Vibrational Spectroscopic Characterization, Inorg. Chem. 60 (2021) 8640–8650, https://doi.org/10.1021/ACS.INORGCHEM.1C00616/SUPPL_FILE/IC1C00616_SI_001.PDF
[39] H. Karzel, W. Potzel, M. Köfferlein, W. Schiessl, M. Steiner, U. Hiller, G. Kalvius, D. Mitchell, T. Das, Lattice dynamics and hyperfine interactions in ZnO and ZnSe at high external pressures, Phys. Rev. B - Condens. Matter Mater. Phys. 53 (1996) 11425–11438, https://doi.org/10.1103/PhysRevB.53.11425
[40] S.F. Mayer, J.E. Rodrigues, C. Marini, M.T. Fernández-Díaz, H. Falcón, M.C. Asensio, J.A. Alonso, A comprehensive examination of the local-and long-range structure of Sb 6 O 13 pyrochlore oxide, 2020. https://doi.org/10.1038/s41598–020–73860–0.
[41] M. Jansen, Die Kristallstruktur von Antimon(V)-oxid, Acta Crystallogr, Sect. B Struct. Crystallogr. Cryst. Chem. 35 (1979) 539–542, https://doi.org/10.1107/S056774087900409X/FULL
[42] J.R. Gavarri, Evolution structurale d′oxydes isomorphes MeX2O4: Relation entre dilatation, vibrations et rigidite, J. Solid State Chem. 43 (1982) 12–28, https://doi.org/10.1016/0022-4596(82)90210-9
[43] G. Schon, Elsevier Scientific Publishing, J. Electron Spectros. Relat. Phenomena 2 (1973), pp. 75–86, https://doi.org/10.1016/0006-8993(75)90185-7
[44] M. Oku, T. Suzuki, Degradation of cleaved LnSb(Ln = La, Ce) by reaction in ultrahigh vacuum and air, Surf. Interface Anal. 21 (1994) 238–244, https://doi.org/10.1002/SIA.740210405
[45] B.L. Zhu, C.S. Xie, D.W. Zeng, W.L. Song, A.M. Wang, Investigation of gas sensitivity of Sb-doped ZnO nanoparticles, Mater. Chem. Phys. 89 (2005) 148–153, https://doi.org/10.1016/j.matchemphys.2004.08.028
[46] R.G. Haverkamp, A.T. Marshall, B.C.C. Cowie, Energy resolved XPS depth profile of (IrO2, RuO2, Sb2O5, SnO2) electrocatalyst powder to reveal core-shell nanoparticle structure, Surf. Interface Anal. 43 (2011) 847–855, https://doi.org/10.1002/SIA.3644
[47] R. Izquierdo, E. Sacher, A. Yelon, X-ray photoelectron spectra of antimony oxides, Appl. Surf. Sci. 40 (1989) 175–177, https://doi.org/10.1016/0169-4332(89)90173-6
[48] H. Bryngelsson, J. Eskhult, L. Nyholm, M. Herranen, O. Alm, K. Edström, Electrodeposited Sb and Sb/Sb2O3 nanoparticle coatings as anode materials for Li-ion batteries, Chem. Mater. 19 (2007) 1170–1180, https://doi.org/10.1021/CM0624769/ASSET/IMAGES/LARGE/CM0624769F00008.JPEG
[49] D.J. Morgan, Metallic antimony (Sb) by XPS, Surf. Sci. Spectra 24 (2017) 024004, https://doi.org/10.1116/1.4994636
[50] G.W. Cong, W.Q. Peng, H.Y. Wei, X.X. Han, J.J. Wu, X.L. Liu, Q.S. Zhu, Z.G. Wang, J.G. Lu, Z.Z. Ye, L.P. Zhu, H.J. Qian, R. Su, C.H. Hong, J. Zhong, K. Ibrahim, T.D. Hu, Comparison of valence band x-ray photoelectron spectrum between Al-N-co-doped and N-doped ZnO films, Appl. Phys. Lett. 88 (2006) 2004–2007, https://doi.org/10.1063/1.2171804
[51] M.M. Gawlik, B. Wiese, A. Welle, J. González, V. Desharnais, J. Harmuth, T. Ebel, R. Willumeit-Römer, Acetic acid etching of Mg-xGd alloys, Met. (Basel) 9 (2019) 117, https://doi.org/10.3390/met9020117
[52] Ü. Özgür, Y.I. Alivov, C. Liu, A. Teke, M.A. Reshchikov, S. Doğan, V. Avrutin, S.J. Cho, H. Morkç, A comprehensive review of ZnO materials and devices, J. Appl. Phys 98 (2005), pp. 1–103, https://doi.org/10.1063/1.1992666
[53] V. Srikant, D.R. Clarke, On the optical band gap of zinc oxide, J. Appl. Phys. 83 (1998) 5447–5451, https://doi.org/10.1063/1.367375